Lithos 266–267 (2016) 182–201

Contents lists available at ScienceDirect

Lithos

journal homepage: www.elsevier.com/locate/lithos

# Mineralogical evidence for lamproite magma mixing and storage at mantle depths: Socovos fault lamproites, SE Spain

A. Cambeses [a,*], A. Garcia-Casco [a,b], J.H. Scarrow [a], P. Montero [a], L.A. Pérez-Valera [c], F. Bea [a]

[a] Department of Mineralogy and Petrology, Faculty of Sciences, University of Granada, Campus Fuentenueva s/n, 18002 Granada, Spain
[b] Instituto Andaluz de Ciencias de la Tierra (CSIC-UGR), Av. Las Palmeras, 4, 18100, Armilla, Granada, Spain
[c] Centro de Estudios Avanzados en Ciencias de la Tierra, University of Jaen, Campus Las Lagunillas s/n, 23071 Jaén, Spain

ARTICLE INFO

*Article history:*
Received 5 July 2016
Accepted 5 October 2016
Available online 15 October 2016

*Keywords:*
Ultrapotassic rocks
Mantle magma mixing
Mediterranean Neogene magmatism
Phlogopite major and trace elements
X-ray maps

ABSTRACT

Detailed textural and mineral chemistry characterisation of lamproites from the Socovos fault zone, SE Spain Neogene Volcanic Province (NVP) combining X-ray element maps and LA-ICP-MS spot analyses has provided valuable information about mantle depth ultrapotassic magma mixing processes. Despite having similar whole-rock compositions, rocks emplaced in the Socovos fault are mineralogically varied: including type-A olivine-phlogopite lamproites; and type-B clinopyroxene-phlogopite lamproites. The Ol-lacking type-B predates Ol-bearing type-A by *c.* 2 million years. We propose that the mineralogical variations, which are representative of lamproites in the NVP as a whole, indicate mantle source heterogeneities. Major and trace element compositions of mineral phases suggest both metasomatised harzburgite and veined pyroxenite sources that were most likely closely spatially related. Thin section scale textural and compositional variations in mineral phases reveal heterogeneous mantle- and primitive magma-derived crystals. The variety of crystals points to interaction and mingling-mixing of ultrapotassic magma batches at mantle depths prior crustal emplacement. The mixing apparently occurred in a mantle melting zone with a channelised flow regime and localised magma chambers-reservoirs. Magma interaction was interrupted when the Socovos and other lithosphere-scale faults tore down to the mantle source region, triggering rapid ascent of the heterogeneous lamproite magma.



## 1. Introduction

Combined mineralogical, textural and compositional characterisation of rocks provides direct critical information for understanding differentiation processes in open magmatic systems (e.g., Barton et al., 1982; Dobosi and Fodor, 1992; Griffin et al., 2002; Streck, 2008). In mantle-derived magmas characterisation of ultramafic source-derived, magma-derived and complex mixed-origin minerals is key to deciphering petrogenetic processes including: melting, mixing and storage (e.g., Grützner et al., 2013; Larsen and Pedersen, 2000; Mitchell, 2008). Ultrapotassic magmas are particularly interesting in this respect because of their heterogeneous primitive character (cf., Rock, 1991). They have compositionally diverse whole-rock compositions, e.g., high-Mg, high-K and enrichment in incompatible elements, and varied mineralogy e.g., olivine, clinopyroxene and phlogopite (cf., Mitchell and Bergman, 1991).

Whole-rock and mineral element and isotopic data indicate that ultrapotassic magma generation is generally related to melting of heterogeneous mantle sources including i) metasomatised refractory depleted harzburgite (e.g., Foley et al., 1986; Jaques et al., 1984; Prelević and Foley, 2007; Venturelli et al., 1988) and ii) mica-amphibole-bearing harzburgite or pyroxenite-veins formed as a consequence of mantle metasomatism by continental sediment-derived fluids or melts (e.g., Arima and Edgar, 1983; Foley, 1992a, 1992b). In addition, geochemical studies have identified variable amounts of both subcontinental lithospheric and asthenospheric mantle end-members in some ultrapotassic magmas, particularly those from the Mediterranean region (cf., Cvetković et al., 2013; Prelević et al., 2008, 2013). Characteristics of sources are reflected in the composition of ultrapotassic magmas, which are typically enriched in incompatible trace elements and have extreme radiogenic Nd-, Sr-, Pb- and Hf-isotope compositions (e.g., Conticelli et al., 2009; Mitchell and Bergman, 1991; Prelević et al., 2008; Venturelli et al., 1984). The varied sources identified for ultrapotassic rocks, in particular lamproites, point to the formation of heterogeneous magmas in a given mantle melting zone. So magma mingling-mixing at mantle depths may be contemplated (Azzone et al., 2013; Conticelli et al., 2011).

Nevertheless, even though petrographic and textural relationships of lamproite minerals provide a powerful tool to study magmatic processes at mantle depths, direct mineralogical evidence of lamproite magma mingling-mixing is scarce. Only a few studies have demonstrated the potential importance of major and trace element mineral chemistry for identifying the mingled-mixed nature of heterogeneous mantle-derived magmas (Semiz et al., 2012; Ubide et al., 2014a, 2014b; Xu et al., 2003). For this reason, in this work we focus on textural-mineralogical characteristics of lamproite magmas s.s. in search of evidence for magma mingling-mixing processes at mantle depths. The lamproites that we investigate

* Corresponding author.
*E-mail address:* aitorc@ugr.es (A. Cambeses).

http://dx.doi.org/10.1016/j.lithos.2016.10.006
0024-4937/

here were emplaced directly from mantle depths by the Socovos fault in the SE Spain Neogene Volcanic Province (NVP) (Fig. 1A; Pérez-Valera et al., 2013). These rocks formed as a result of Late Miocene mantle melting related to regional uplift, subsequent extension and associated asthenosphere upwelling that has continued to the present day in the westernmost Mediterranean (cf., Duggen et al., 2005; Mancilla et al., 2015; Palomeras et al., 2014). The Socovos fault lamproites were selected for detailed mineralogical-textural study because of their notable lack of evidence of interaction with the continental crust during ascent and emplacement. They, therefore, represent the perfect candidates for characterising mantle-related petrogenetic processes of primitive lamproite magmas.

Here we are interested in the detailed textural and chemical description and characterisation of the diverse associations of petrogenetic minerals that coexist even at the scale of a single thin section. In order to facilitate the search for mineral complexities we rastered areas of thin

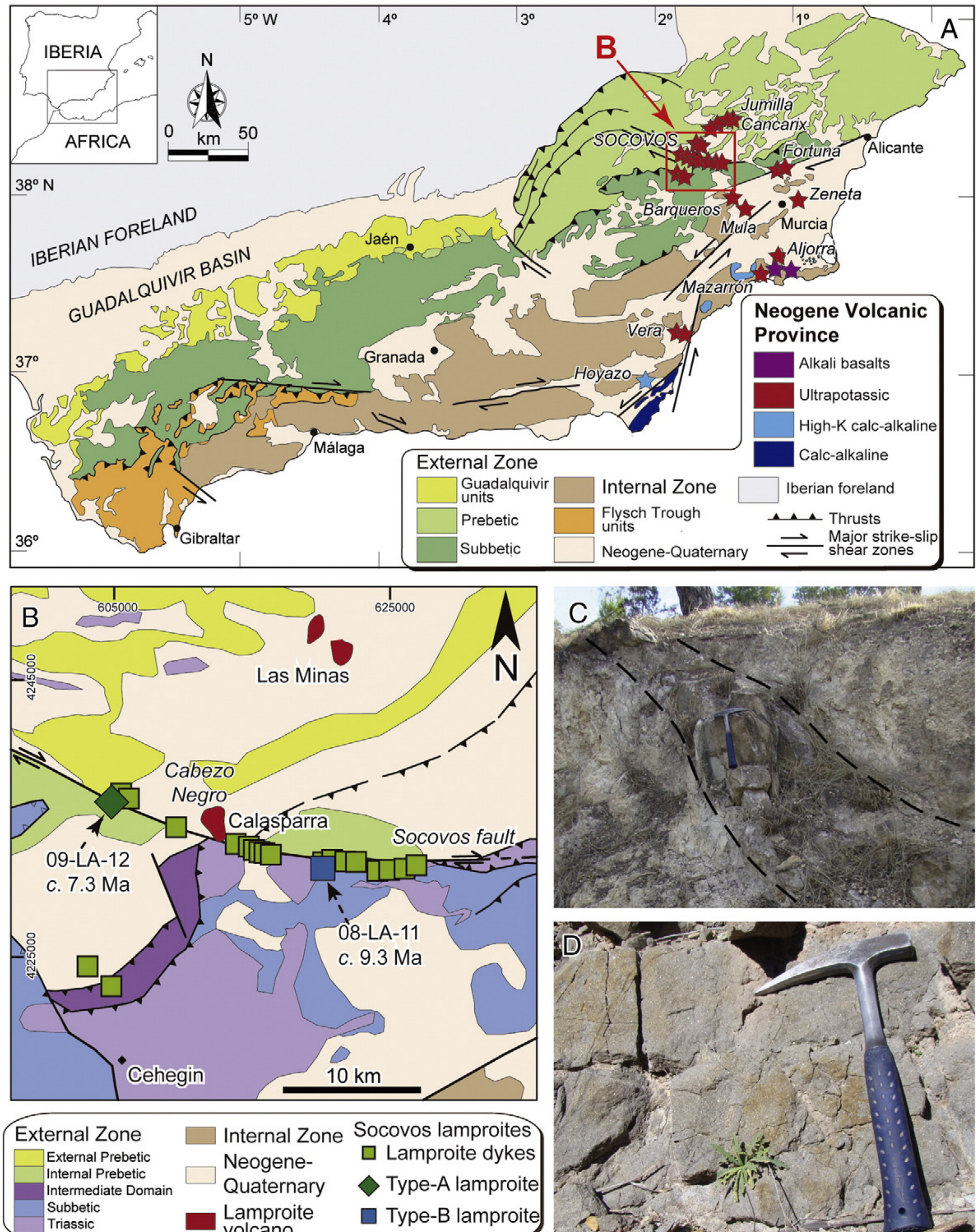


**Fig. 1.** A) Geological map of the Betic cordillera (modified from Comas et al., 1999) showing major strike–slip faults and shear zones and lamproite localities in the SE Spain Neogene Volcanic Province (modified López-Ruiz and Rodriguez-Badiola, 1980). B). Geological map of Socovos fault showing lamproite occurrences and major geological structures (modified of Pérez-Valera et al., 2013). The distribution of lamproitic dykes along the fault and other lamproitic outcrops from Casalasparra and studied samples are shown in C) and D); 09-LA-12 (type-A lamproite) located in eastern fault sector (*c.* 7.3 Ma) and 08-LA-11 (type-B lamproite) in western fault sector (*c.* 9.3 Ma).

sections to produce large elemental X-ray maps. Pertinent manipulation of raw X-ray signals allowed quantification of mineral chemistry permitting identification of compositional variations including zoning and also the textural positions of key minerals. When compared with standard optical and BSE images, X-ray maps have the advantage of being multi-element (multi-channel) analyses, which permit rapid identification of subtle, though petrogenetically significant, chemical-textural characteristics of coexisting minerals. This methodology provides a firm basis for careful selection of LA-ICP-MS trace element spot analyses. In this way, we aim to characterise the heterogeneous mantle sources and melts involved in the formation of lamproite magmas and their mingling-mixing and differentiation processes at mantle depths.

As shown below, our approach confirms the rather heterogeneous nature of lamproite magmas from the mm- to the km-scale. The coexistence of minerals with significantly different origins, including crystals from varied mantle sources and magmas, at the mm-scale confirms magma mingling-mixing at mantle depths. These heterogeneous mineral associations also allow characterisation of the elevated rates at which high temperature processes of magma generation, storage, mingling-mixing and ascent proceeded in the mantle.

## 2. Geological setting

The Tertiary Betic Orogen in the Western Mediterranean is related to closure of the Tethys ocean and syn- to tardi-orogenic development of new oceanic-continental basins. The orogen is divided into two main zones: the External Zone to the north, the South-Iberian paleomargin, and the Internal Zone to the south, the Alboran Domain (Fig. 1A). The South-Iberian paleomargin comprises a fold and thrust belt of Triassic to Miocene sedimentary rocks with two principal groups of units: the Subbetic and Prebetic (Fig. 1A) (e.g., García-Hernández et al., 1980). The Alboran Domain is made up of a stack of tectonic units which comprise Paleozoic to Mesozoic rocks affected by Alpine and pre-Alpine deformation and metamorphism (e.g., Platt et al., 2013). Its units are, from bottom to top: the Nevado-Filábride Complex; the Alpujárride Complex; and the Malágide Complex (Fig. 1). Late Miocene to Quaternary sedimentary rocks unconformably overlie both the Internal and External zones (Fig. 1A; e.g., Sanz de Galdeano and Vera, 1992). Since the Upper Miocene strong strike-slip faulting has affected the region causing displacement of tectonic blocks and favouring the emplacement of SE Spain Neogene Volcanic Province (NVP) magmas (Fig. 1A).

The age of emplacement of NVP magmas ranges from 11 to 17 Ma for the calc-alkaline rocks of Cabo de Gata (López-Ruiz and Rodriguez-Badiola, 1980; Zeck et al., 1998). Followed by the 9–12 Ma high-K calc-alkaline rocks of Mar Menor and Mazarrón (Cesare et al., 2009; López-Ruiz and Rodriguez-Badiola, 1980) and the 6–9 Ma high-K calc-alkaline rocks of El Hoyazo volcano (Cesare et al., 2003, 2009; Zeck and Williams, 2002). The ultrapotassic rocks were emplaced at 6–9 Ma (Duggen et al., 2005; Kuiper et al., 2006; Pérez-Valera et al., 2013). The youngest magmatic rocks in the region are alkali basalts, 2–3 Ma (Bellon et al., 1983; Duggen et al., 2005).

Ultrapotassic magmas of the NVP were emplaced, in general, as volcanoes, through plugs and dykes crosscutting the late Tertiary sedimentary cover and the basement of both the Betic External and Internal Zones (Seghedi et al., 2007; Venturelli et al., 1984). The distribution of ultrapotassic rocks is associated with fault-bounded basin margins that are filled by Neogene marine-to-continental sediments (Fig. 1A; Fuster, 1967; López-Ruiz and Rodriguez-Badiola, 1980). Effusive massive lavas, peperitic breccias and pyroclastic rocks are present in volcanic structures of 0.5–1 km diameter (Cambeses and Scarrow, 2013; Fuster, 1967; Playà and Gimeno, 2006). The main edifices crop out in Cancarix, Barqueros and Vera (e.g., Seghedi et al., 2007; Gernon et al., 2015; Fig. 1A). Dykes and plugs have variable dimensions and are often related to strike-slip faults, as in Puebla de Mula (Fuster, 1967; Venturelli et al., 1984) Fortuna (Bellon et al., 1983; Kuiper et al., 2006) and Socovos (Pérez-Valera et al., 2013).

## 3. Socovos lamproites

The Socovos fault ultrapotassic rocks, are mostly emplaced as dykes along fractures parallel to principal fault planes, Riedel faults and tension gashes (Pérez-Valera et al., 2013). The dykes are up to 2 km long and up to 10 m thick, increasing in general to the East. They are unevenly distributed along the whole lateral extent of the fault with a cluster over some 20 km in the central section close to Calasparra (Fig. 1B). Cabezo Negro is the only volcanic edifice identified, so far, along the fault (Fig. 1B). The ultrapotassic rocks intrude Triassic carbonates to Upper Miocene marls of the Betic External Zone (Subbetic). Eastern Socovos dykes have older ages (8.2–9.3 Ma, Ar–Ar phlogopite) than those in the west (*c.* 7.2 Ma, Ar–Ar phlogopite) (Pérez-Valera et al., 2013). The eastern sector dykes are the oldest ultrapotassic rocks in the NVP, whereas those of the western sector yield ages similar to the other ultrapotassic NVP rocks (Duggen et al., 2005).

Socovos lamproites are microporphyritic, holo- to hypocrystalline and with rare vesicular textures. The main minerals are olivine (locally up to 5 mm, commonly altered), clinopyroxene and phlogopite. The matrix is formed of sanidine, scarce glass and accessory apatite, chromite, amphibole and ilmenite (Pérez-Valera et al., 2013).

Socovos rocks are lamproites *ss.* (Pérez-Valera et al., 2013). They are alkaline ($Na_2O + K_2O \approx 9.5–11.0$ and $SiO_2 \approx 56.3–62.0$), peralkaline, perpotassic and ultrapotassic with molar $(K_2O + Na_2O) / Al_2O_3 \approx 1.02–1.41$, $K_2O/Al_2O_3 \approx 0.9–1.1$ and molar $K_2O/Na_2O \approx 5.5–4.5$ (Supplementary Fig. S1).

The Socovos lamproites have major element compositions typical of lamproites from the NVP, with high MgO (5.0–12.9 wt%), $K_2O$ (9.1–10.5 wt%) and $P_2O_5$ (0.6–1.6 wt%), moderate $TiO_2$ (1.5–1.8 wt%) and $FeO_T$ (3.9–5.3 wt%) and low $Al_2O_3$ (8.7–10.9 wt%), CaO (2.1–5.9 wt%) and $Na_2O$ (0.2–1.6 wt%) (Supplementary Fig. S2). These features are similar to nearby lamproitic outcrops for example Jumilla, Calasparra and Cancarix (cf., Conticelli et al., 2009; Duggen et al., 2005; Pérez-Valera et al., 2013; Venturelli et al., 1984). Socovos trace element values such as high Ba (1276–3892 ppm), Zr (848–1013 ppm) and Sr (515–1685 ppm,) (Supplementary Figs. S3 and S4) are characteristic of lamproites (Mitchell and Bergman, 1991). More specifically, they have high Th (108–220 ppm) and low V (71–110 ppm) contents, typical of Spanish lamproites (Supplementary Figs. S3 and S4; cf. Venturelli et al., 1984; Duggen et al., 2005; Prelević et al., 2008). The isotopic compositions of the Socovos lamproites show a clear enriched character, with $^{87}Sr/^{86}Sr_{9Ma} = 0.71706–0.72068$ and high negative values of $\varepsilon Nd_{9Ma} = -11$ to $-12$ (Supplementary Fig. S5), again typical of NVP lamproites (cf., Conticelli et al., 2009; Duggen et al., 2005; Prelević et al., 2008).

## 4. Material and methods

Here we consider the mineralogy of two Socovos fault lamproite dykes described by Pérez-Valera et al. (2013) emplaced along the Socovos fault (Fig. 1B). The selected dykes are representative of the mineral and whole-rock compositional and geochronological ranges present along the fault:

i.- Sample 09-LA-12 is a younger dyke, *c.* 7.3 Ma, located in the western sector of the fault and corresponds to type-A lamproite (see below and Fig. 1B). It is less than *c.* 10 m long and 4–1 m wide (Fig. 1C). It is affected by post-emplacement fault movements.

ii.- Sample 08-LA-11 emplaced in the eastern sector is an older intrusion, *c.* 9.3 Ma, it corresponds to type-B lamproite (see below and Fig. 1D). It is *c.* 20 m long and 0.5–2 m wide.

Analytical methods (EMPA and LA-ICP-MS) are summarised in Supplementary Material I. Major and trace element mineral data are given in Supplementary Material II and III, respectively.

## 5. Petrography and mineral chemistry

The terms phenocryst and groundmass crystals are used here as a textural description of magma-derived medium-fine and fine-grained crystals respectively. On the other hand, the term megacryst is a textural description of larger crystals but without any genetic implication. Crystals not in equilibrium with the groundmass but to a certain extent genetically related to the lamproitic magma are generally described as antecrysts (e.g., Davidson et al., 2007), The term xenocrysts is used to describe ultramafic rock-derived crystals (e.g. Prelević and Foley, 2007), here it refers to all crystals derived from the ultramafic mantle source(s) or at the wall-rock(s) through which the magma rose.

Pérez-Valera et al. (2013) classified all the Socovos volcanic rocks as olivine-phlogopite lamproites. However, the petrographic characteristics pinpoint important variations in terms of phase abundances that permit us to classify the Socovos rocks into two types:

i- Type-A contains large porphyritic olivine and phlogopite set in a groundmass composed of clinopyroxene, amphibole and sanidine and accessory apatite, magnesiochromite-chromite and ilmenite (Fig. 2). This type is represented by sample 09-LA-12.

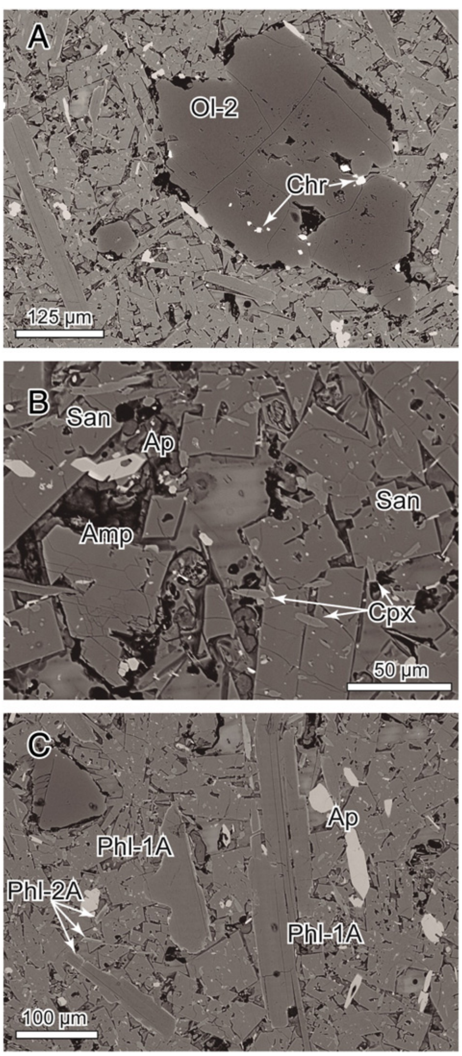


**Fig. 2.** Back-scattered electron images showing the phases relationship of type-A lamproite. A) Olivine phenocryst (Ol-2) with chromite inclusions. B) Ground-mass phases. C) Medium sized phlogopite Phl-1A and rims and small phenocryst of phlogopite Phl-2A. Ol: olivine; Phl: phlogopite; Cpx: clinopyroxene; Amp: amphibole; San; sanidine; Ap; apatite; and Chr: chromite.

ii- Type-B has porphyritic phlogopite and clinopyroxene set in a groundmass of phlogopite and sanidine with apatite as the principal accessory phase (Fig. 3). This type is represented by sample 08-LA-11.

Hence, the main observation is that phenocrystic olivine and clinopyroxene are mutually exclusive and the rocks can be classified as olivine-phlogopite, type-A, and clinopyroxene-phlogopite, type-B, lamproites.

### 5.1. Olivine

Two generations of olivine are present in the type-A lamproite (Figs. 4 and 5). Megacrystic anhedral xenocrysts (2–4 mm) with variably deformed internal structures e.g., kinked grains characterise Ol-1 (Fig. 5). On the other hand, Ol-2 are subhedral phenocrysts with variable, but generally smaller, grain size (0.2–1 mm) and, in some crystals, inclusions of magnesiochromite-chromite (Figs. 2A and 5). Neither olivine type has reaction rims.

Olivine has a variable composition Olivine Ol-1 has limited variation in forsterite content, $Fo_{89–91}$, with the higher values at crystal rims (Fig. 4). Olivine Ol-2 is characterised by higher forsterite content, $Fo_{92–95}$ (Fig. 4). Detailed X-ray mapping of major and minor element compositions revealed variation. In Ol-1 the Fo-poorer cores have 0.01–0.04 wt% CaO, 0.00–0.04 wt% $Cr_2O_3$ and 0.4–0.5 wt% NiO (Figs. 4 and 5). In Ol-2 and the rims of Ol-1 these elements have more elevated concentrations: CaO (0.05–0.08 wt%), $Cr_2O_3$ (0.05–0.2 wt%) and NiO-(0.4–0.8 wt%) (Figs. 4 and 5). Similarly, the two olivine types have variable trace elements concentrations (Fig. 7). The Fo-poorer Ol-1 has relatively high Co (127–161 ppm), moderate Ni (3062–3635 ppm) and Li (2–11 ppm) and low Sc (0.4–6.6 ppm), V (1.6–5.7 ppm) and P (28–95 ppm) (Fig. 4). However, Ol-1 rims and Ol-2 are enriched in Ni (4288–6599 ppm), Li (22–30 ppm), Sc (2.5–4.8 ppm), V (5.3–11.5 ppm) and P (159–456 ppm) and depleted in Co (115–125 ppm) (Fig. 4).

### 5.2. Clinopyroxene

Clinopyroxene is common to both types of lamproite, it shows textural and compositional variations.

In the type-A lamproite clinopyroxene is only present in the groundmass, it forms tabular subeuhedral crystals (15–25 μm; Fig. 2B). They have a composition of augite $Wo_{40–43}$-$En_{50–51}$-$Fs_{6–8}$ (Mg# ≈ 88–90) and intermediate $Cr_2O_3$ (0.01–0.59 wt%) and $Al_2O_3$ (0.23–1.18 wt%) and high $TiO_2$ (0.7–1.0 wt%) (Fig. 6).

In the type-B lamproite clinopyroxene forms tabular euhedral phenocrysts (200–30 μm) (Fig. 3A, B and F). The clinopyroxenes are augites ($Wo_{42–46}$-$En_{50–53}$-$Fs_{3–5}$, Fig. 6A). The X-ray maps illustrate the textural-compositional variations with similar range in $Al_2O_3$ (0.05–0.28) but particularly variable $TiO_2$ and $Cr_2O_3$ (Fig. 7). These differences allow identification of three clinopyroxene populations:

i.- Cpx-1 (Mg# ≈ 91–92%) has $TiO_2$ (0.26–0.38 wt%) and $Cr_2O_3$ (0.04–0.24 wt%) (Figs. 6 and 7). Notably, this composition forms the cores of coarse- and medium-grained phenocrysts which include phlogopite phenocrysts (Fig. 3A).

ii.- Cpx-2 (Mg# ≈ 92–93%) is richer in $TiO_2$ (0.41–0.48 wt%) and $Cr_2O_3$ (0.53–0.61 wt%). It forms the rims of Cpx-1 phenocrysts and small phenocrysts (Figs. 6 and 7).

iii.- Cpx-3 (Mg# ≈ 92–93%) has a higher content in $TiO_2$ (0.38–0.48 wt%) and $Cr_2O_3$ (0.47–0.84 wt%) than Cpx-1 phenocrysts (Figs. 6 and 7). Locally, rims of Cpx-3 are depleted in $Cr_2O_3$ (0.22–0.29 wt%) (Figs. 6 and 7). This type of clinopyroxene forms inclusion-free medium-grained phenocrysts (Fig. 3B).

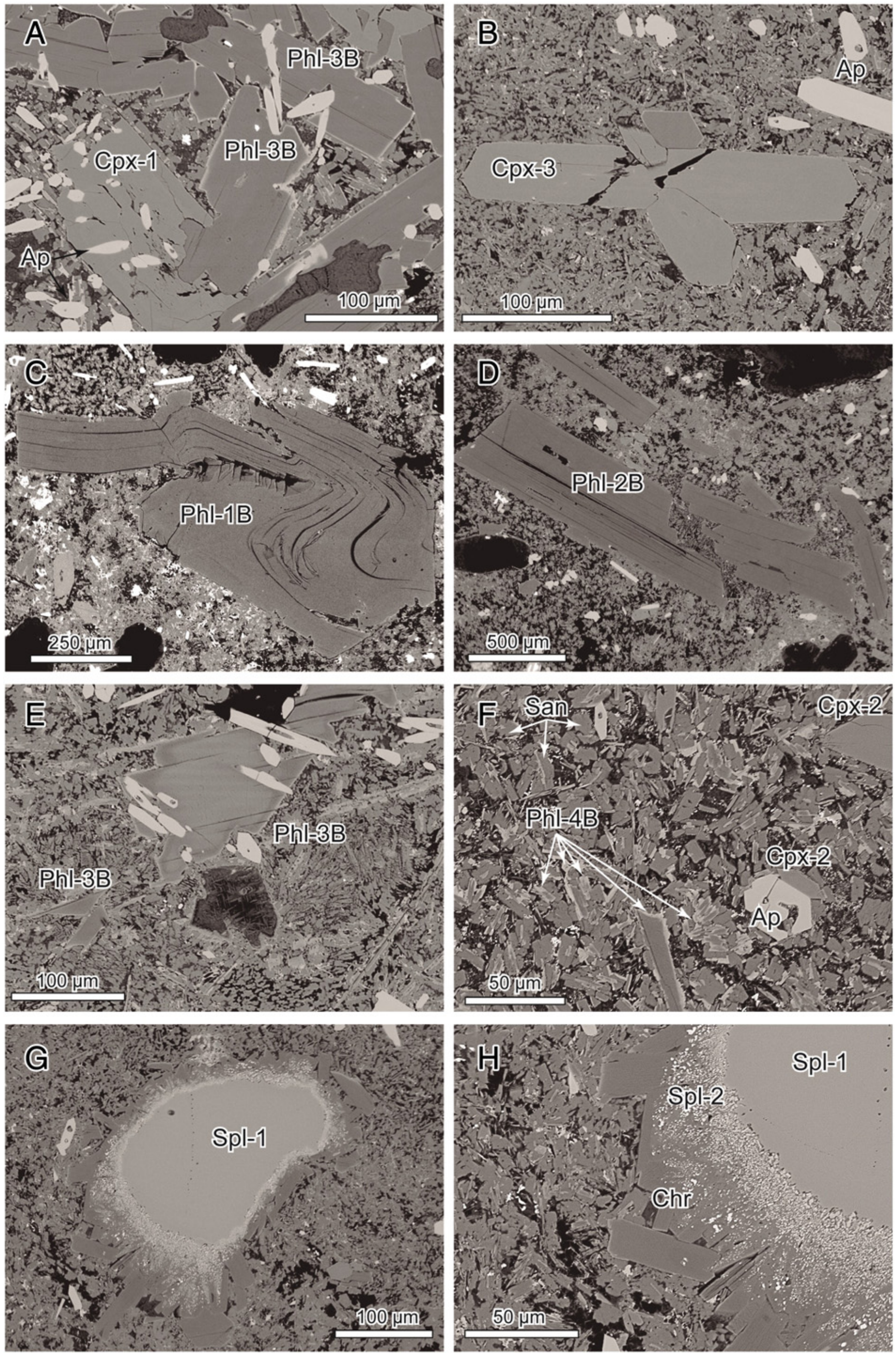


**Fig. 3.** Back-scattered electron images showing the phases relationship of type-B lamproite. A) and B) Textural relations of clinopyroxenes. C) Large deformed mantle derived xenocryst Phl-1B. D) Euhedral megacrysts Phl-2B. E) Euhedral phenocryst containing inclusions of groundmass phases. F) Microphenocrysts Phl-4B included in groundmass. G) Large-sized xenocrystic spinel. H) Detail of disequilibrium textures in xenocrystic spinel characterised by a progressive compositional shift towards chromite at the grain rims. Phl: phlogopite; Cpx: clinopyroxene; San; sanidine; Ap; apatite; Spl: spinel; and Chr: chromite.

### 5.3. Amphibole

Amphibole is only found as a groundmass phase in the type-A lamproite (Fig. 2B). It has a restricted richterite composition (Supplementary Fig. S6) with $TiO_2 \approx 3$–5 wt% and $Na_2O \approx 4$–5 wt%.

### 5.4. Phlogopite

Phlogopite is ubiquitous in the Socovos lamproites. In the studied samples it shows the largest textural and compositional variations of all minerals, and important differences occur as a function of lamproite type.

In the type-A lamproite phlogopite forms 500–100 μm euhedral phenocrysts. Large phlogopite crystals have inclusion-free cores whereas the rims and smaller crystals contain groundmass phases, such as apatite. Phlogopite has uniform $K_2O$ (10.1–10.5 wt%) but compositional variations in other components that allows the following textural-chemical classification:

i.- Phl-1A (A refers to type-A lamproite) are large phenocrysts with cores rich in Mg (Mg# $\approx$ 93–94) and restricted $Al_2O_3$ (11.8–12.2 wt%), $FeO_T$ (2.7–3.1 wt%) and $TiO_2$ (2.1–2.4 wt%) (Figs. 5F, E and 8). The rims of Phl-1A are slightly poorer in Mg (Mg# $\approx$

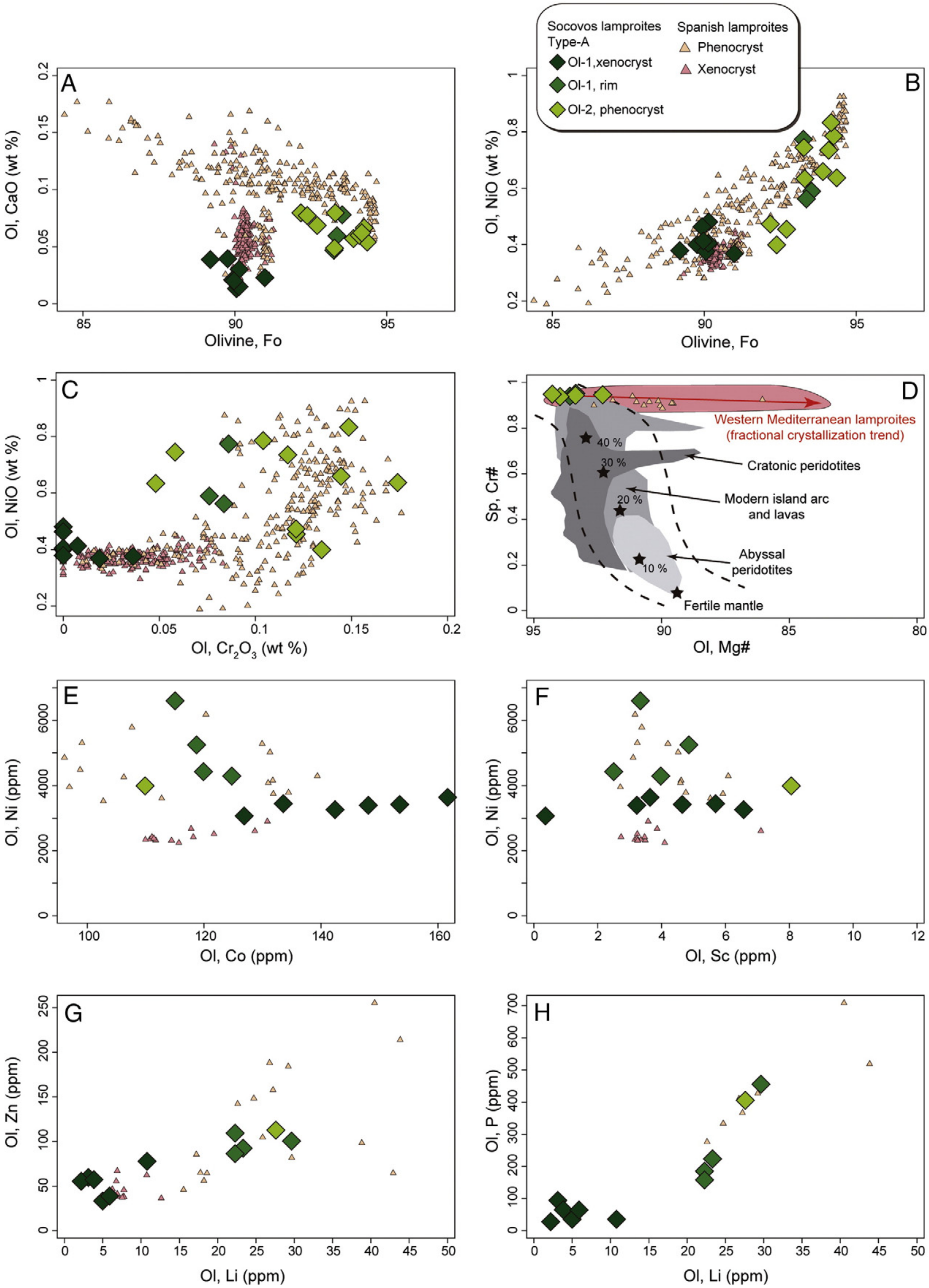


**Fig. 4.** Compositional variation of olivine from type-A lamproite and other Spanish lamproites for comparison (smaller and lighter symbols; data from Venturelli et al., 1984, 1988; Prelević and Foley, 2007; Prelević et al., 2013) A) CaO vs Fo#, B) NiO vs Fo, C) NiO vs $Cr_2O_3$. D) Olivine-spinel pairs plotted on the olivine-spinel mantle array (OSMA). Western Mediterranean field, cratonic peridotites, modern island arc lavas and abyssal peridotites from Prelević and Foley, (2007) and Prelević et al., (2013). E) Ni vs Co. F) Ni vs Sc. G) Zn vs Li. H) P vs Li.

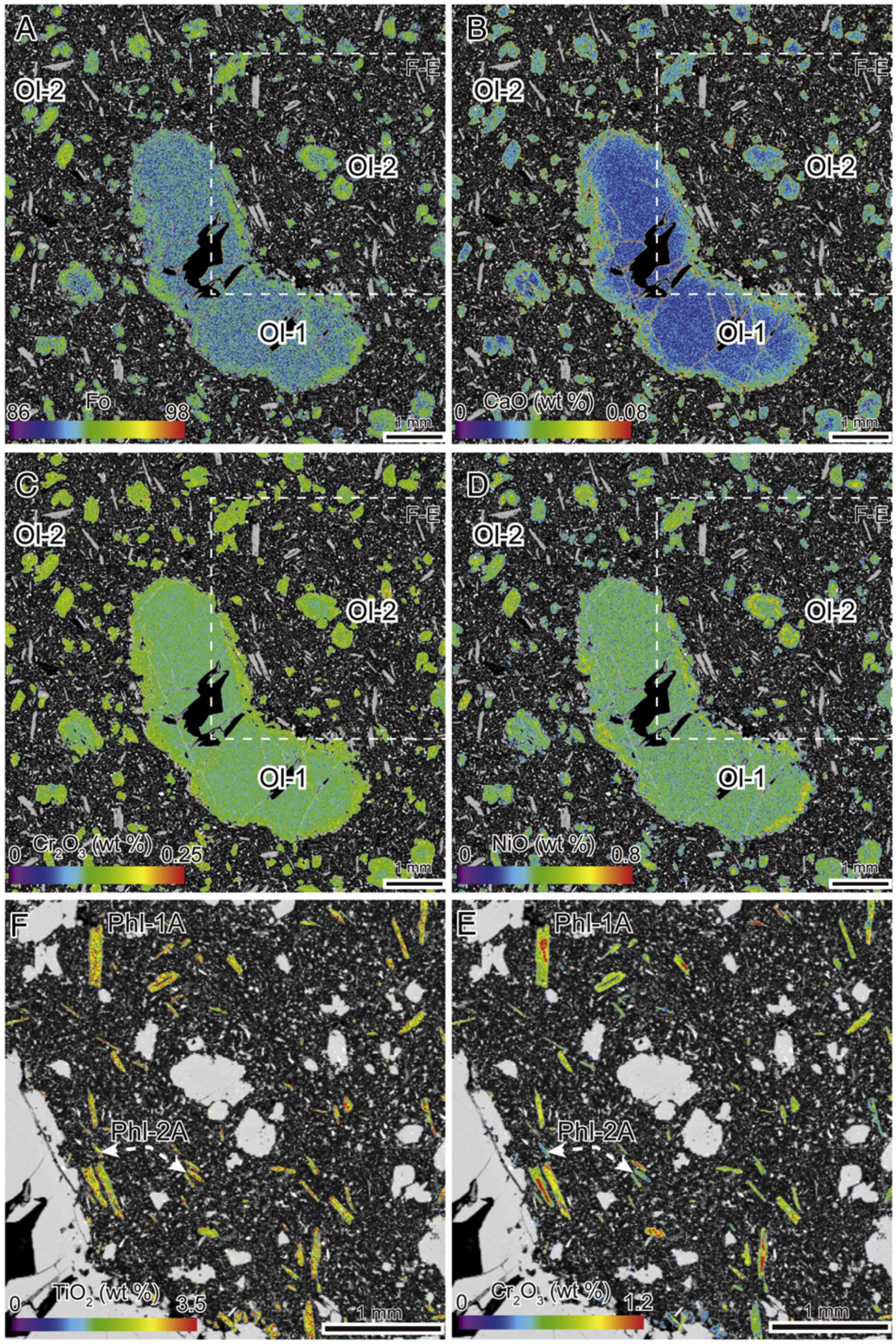


**Fig. 5.** Composite X-ray images of type-A lamproite. A) to D) show Fo molar%, CaO wt%, $Cr_2O_3$ wt%, and NiO wt% (see Supplementary Material I for procedures). F) and E) insets showing $TiO_2$ wt% and $Cr_2O_3$ wt% contents of micas. Ol-1, Ol-2, Phl-1A and Phl-2A are indicated. The images are masked in order to show olivine set in a base layer of the corresponding backscattered electron image that shows the basic textural features of the scanned areas.

91–93) and $Al_2O_3$ (11.0–11.5 wt%) and richer in $FeO_T$ (3.4–4.0 wt%) and $TiO_2$ (2.7–3.4 wt%) (Figs. 5F, E and 8). A wide $Cr_2O_3$ compositional variation is detected, with phlogopite Phl-1A cores and rims having, respectively, higher (1.0–1.5 wt%) and lower (0.65–0.78 wt%) concentrations (Figs. 5F, E and 8).

ii.- Phl-2A forms small phenocrysts which may contain inclusions of groundmass phases. They have compositions similar to the Phl-1A rims (Mg# ≈ 90–92; 11.0–11.6 wt% $Al_2O_3$, 3.5–4.0 wt% $FeO_T$ and 2.9–3.1 wt% $TiO_2$; Figs. 5F, E and 8). The $Cr_2O_3$ is variable (0.13–0.91 wt%), with the lowest values characterising the smallest phenocrysts (Figs. 5F, E and 8).

In the type-B lamproite phlogopite is the principal porphyritic phase. It forms 2 mm to 100 μm euhedral megacrysts to fine-grained groundmass minerals (Fig. 9). Notably, it has some distinctive textures: i) large deformed xenocrysts with kinked morphology and undulose extinction (Fig. 3C); ii) large euhedral megacrysts with resorbed textures (Fig. 3D); iii) tabular euhedral phenocryst locally containing inclusions of groundmass phases (Fig. 3C) and; iv) groundmass crystals included in the groundmass sanidine (Fig. 3F). In terms of major element compositions all the phlogopite have similar $Al_2O_3$ (10.5–11.7 wt%) variable $TiO_2$ (1.2–3.4 wt%) and a wide range in $FeO_T$ (2.0–7.1 wt%) (Fig. 8).

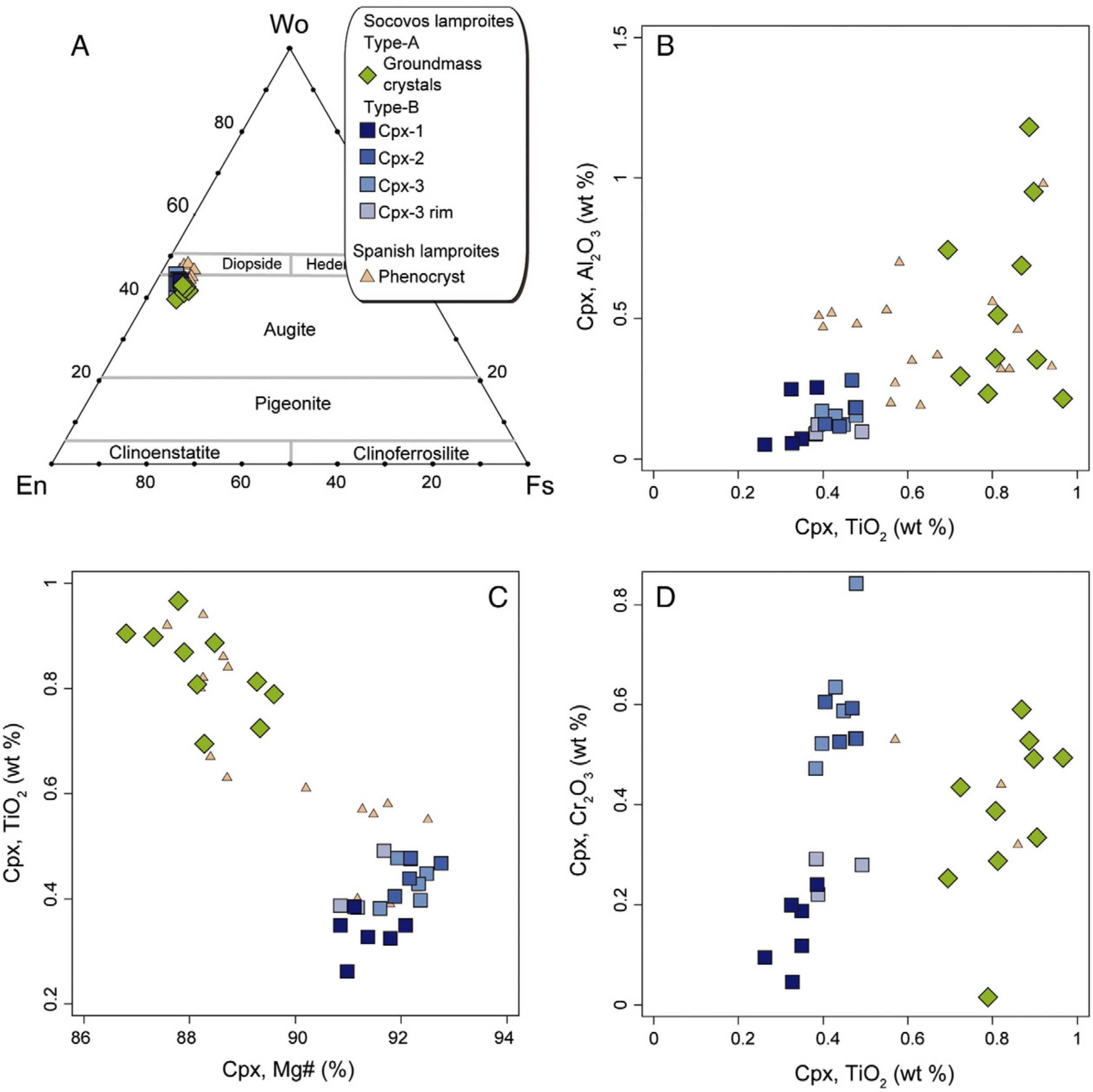


**Fig. 6.** Compositional variations of clinopyroxene from Socovos lamproites and Spanish lamproites (smaller and lighter symbols; data from López-Ruiz and Rodríguez-Badiola 1980; Venturelli et al., 1984, 1988; Contini et al., 1993) A) Classification of pyroxenes in the diagram En-Wo-Fs of Morimoto et al. (1988). B) $Al_2O_3$ vs $TiO_2$. C) $TiO_2$ vs Mg#. D) $Cr_2O_3$ vs $TiO_2$.

The X-ray maps allow the following textural-chemical classification of phlogopite (Fig. 9):

i.- Phl-1B crystals are commonly deformed and fractured (Figs. 3C and 9). These micas are Mg-rich (Mg# ≈ 94–96) with low $Al_2O_3$ (10.8–11.4 wt%), $FeO_T$ (2.1–2.7 wt%) and $TiO_2$ (1.2–1.7 wt%) (Figs. 8 and 9). The crystals are characterised by low $Cr_2O_3$ (0.2–0.9 wt%) (Figs. 8 and 9D) with higher $Cr_2O_3$ contents detected in the rims (Fig. 10). Some phlogopites of this type have complex compositional $Cr_2O_3$ zoning (Fig. 14D). Notably, kinked crystals display oscillatory zoning with alternate low Cr and higher Cr growth bands (Fig. 10.2). The most external parts of the crystal rims (30–40 μm) show significantly higher $TiO_2$ and $FeO_T$ and lower $Al_2O_3$ and $Cr_2O_3$ (Figs. 9 and 10). These external rims are phlogopite type Phl-4B, see below.

ii.- Phl-2B comprises phenocrysts, including large tabular megacryst, with reabsorbed textures, and minor small crystals (Figs. 3D and 9). These micas are Mg-rich (Mg# ≈ 94–96) and have slightly higher values of $Al_2O_3$ (11.3–11.7 wt%) and $FeO_T$ (2.0–3.0 wt%) than Phl-1B (Figs. 8 and 9). Significantly, $TiO_2$ contents (1.2–1.7 wt%) are similar to Phl-1B micas (Figs. 8 and 9). The most distinctive feature of this type of phlogopite is its high $Cr_2O_3$ content (0.6–1.8 wt%) (Figs. 8 and 9). In detail, the distribution of $Cr_2O_3$ contents varies in different crystals. Some crystal have cores with a similar composition to the Phl-1B rims (*c.* 1 $Cr_2O_3$ wt%) whereas the rims are richer in Cr (up to *c.* 1.8 wt%) (Figs. 10 and 11). Other crystals have an antipathetic zoning in $TiO_2$, with Ti-poor Cr-rich cores, which is typical of Phl-2B and Ti-rich and Cr-poor rims, typical of Phl-3B (see below) (Fig. 11). Phologite Phl-2B has thin rims (30–40 μm) rich in $TiO_2$ and $FeO_T$ and poor in $Al_2O_3$ and $Cr_2O_3$. These external rims are phlogopite type Phl-4B (see below; Figs. 9 and 11).

iii.- Phl-3B are medium- to small phenocrysts, although some megacrysts are also recognisable (Figs. 3C and 9). These micas are relatively poor in Mg (Mg# ≈ 90–93) with restricted values of $Al_2O_3$ (10.5–11.2 wt%) and higher $FeO_T$ (3.2–4.5 wt%) and $TiO_2$ (2.0–3.1 wt%) contents than either Phl-1B or Phl-2B (Figs. 8 and 9). The main characteristic of Phl-3B, however, is

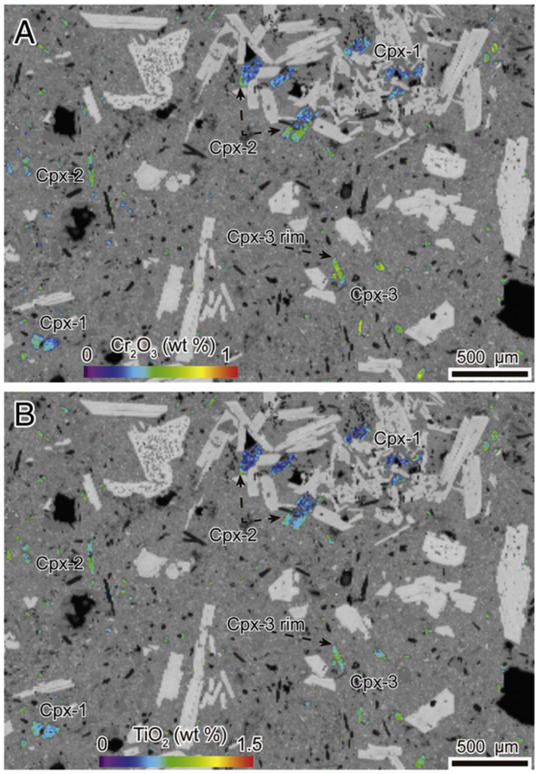


**Fig. 7.** Composite X-ray images of type-B lamproite. A) $Cr_2O_3$ wt% and B) $TiO_2$ wt%. The images are masked in order to show clinopyroxene set in a base layer of the corresponding backscattered electron image that shows the basic textural features of the scanned area. Cpx-1, Cpx-2 and Cpx-3 are indicated.

the relative enrichment in $TiO_2$ and $FeO_T$ and depletion in $Cr_2O_3$ (0.01–0.5 wt%) (Figs. 8, 9 and 11). This type of mica rims both large and small phenocrysts of Phl-2B and is present as single homogeneous phenocrysts, that are locally megacrystic (Fig. 11). The most external rims of Phl-3B with notable $FeO_T$ enrichment are phlogopite type Phl-4B (see below; Figs. 9 and 11).

iv.- Phl-4B are groundmass crystals and the aforementioned thin external rims on all the other phlogopite types (Phl-1B, 2B and 3B; Fig. 3F). These micas are Mg-poor (Mg# ≈ 84–88) but have $Al_2O_3$ contents (10.9–11.3 wt%) similar to the other mica types (Figs. 8 and 9). Type Phl-4B is distinctive in being the richest in $FeO_T$ (4.8–7.0 wt%), poorest in $Cr_2O_3$ (0.02–0.1 wt%) of all the micas and slightly richer in $TiO_2$ (2.6–3.9 wt%) than Phl-3B (Figs. 8 and 11).

Trace element distributions in the phlogopite types are distinctive with broad ranges in the concentrations of many trace elements. The beam-size diameter, 80–60 µm, of the LA-ICP-MS, is larger than the type Phl-4B crystals so no data was obtained for that type. Compositional variations are a function of both the type of lamproite as well as the type of phlogopite (Fig. 12).

Type-A lamproite phlogopites have a positive correlation between typically compatible elements, i.e., Cr, V and Ni: Phl-1A has the highest concentrations and Phl-2A the lowest (Fig. 12). Significantly, Phl-1A micas have low Li (22–46 ppm) cores whereas their rims and Phl-2A are richer in Li (50–123 ppm) (Fig. 12). Large ion lithophile elements (LILE) have similar concentrations, in Phl-1A and Phl-2A: Cs (25–44 ppm), Ba (1536–3820 ppm) and Rb (328–516 ppm) (Fig. 12). The concentrations of high field strength elements (HFSE) are low in both type of micas: Nb ≈ 2.3–10.2 ppm and Zr ≈ 2.4–19.6 ppm. They show a positive correlation with the LILE (Fig. 12).

Type-B lamproites main compositional variations in phlogopites are strongly related to Cr content (Fig. 12). High-Cr micas (i.e., types Phl-1B and Phl-2B) have higher Ni (202–908 ppm) and lower V (427–853 ppm) contents than low-Cr Phl-3B mica (Ni ≈ 208–480 ppm; V ≈ 930–1944 ppm; Fig. 12). The concentration in Li (36–84 ppm) is similar in all types of mica (Fig. 12). LILE also show similar concentrations, e.g., in Cs (18–47 ppm) and Ba (3842–5426 ppm), independent of mica type (Fig. 12). However, some LILE concentrations vary between phlogopite types: Rb is depleted in Phl-1B (Rb 372–536 ppm) and Phl-3B (Rb 358–570 ppm) but enriched in Phl-2B (Rb 431–624 ppm) (Fig. 12). The HFSE have variable behaviour, Zr (14–43 ppm), Th (0.0–0.30 ppm) and Hf (0.45–1.25 ppm) are similarly concentrated in all types of micas (Fig. 12). By contrast, Nb is depleted in Cr-rich phlogopite types Phl-1B and Phl-2B (Nb 7–15 ppm) and enriched in Cr-poor Phl-3B mica (Nb 12–27 ppm) (Fig. 12).

### 5.5. Sanidine

Sanidine is common as groundmass crystals in both lamproite types (Figs. 2B and 3F). Its composition is similar in both, $Or_{93-95}$ $Ab_{5-7}$ $An_0$. However, it has variable $FeO_T$ contents 1.2–1.6 wt% in the type-A lamproite and 2.5–2.7 wt% in the type-B lamproite (see Supplementary Fig. S7).

### 5.6. Spinel

Spinel group minerals have only been identified as inclusions in type-A olivine Ol-2 (Fig. 2A). Compositions are magnesiochromite-chromite with 2.1–2.8 wt% $Al_2O_3$, 1.0–1.4 wt% $TiO_2$, 16.2–25.9 wt% $Fe_2O_3$, Cr# ≈ 0.94–0.95 and Mg# ≈ 0.36–0.38 (Supplementary Fig. S8).

Notably, large xenocrystic spinels (200 µm × 100 µm, Fig. 3G) are present in the type-B lamproite. These crystals display disequilibrium textures characterised by a progressive enrichment from chromite coronas to rims (Fig. 3H). The cores are spinel *ss.*, Spl-1, with 47–50 wt% $Al_2O_3$, 16.4–16.9 wt% $Fe_2O_3$, Cr# ≈ 0.22–0.23 and Mg# ≈ 0.67–0.68 (Supplementary Fig. S8). The parts of the coronas nearest the cores, Spl-2, has 25–28 wt% $Al_2O_3$, 0.7–1.4 wt% $TiO_2$, 17.2–19.1 wt% $Fe_2O_3$, Cr# ≈ 0.42–0.47 and Mg# ≈ 0.62–0.63 (Supplementary Fig. S8). The outer coronas and rims of spinel, chromite *ss.* have 1.7–3.5 wt% $Al_2O_3$, 0.8–1.7 wt% $TiO_2$, 19.3–23.9 wt% $Fe_2O_3$, Cr# ≈ 0.91–0.96 and Mg# ≈ 0.42–0.51 (Supplementary Fig. S8).

### 5.7. Ilmenite

Ilmenite is present disseminated in the groundmass of both lamproite types. It has 51–57 wt% $TiO_2$, 24–41 wt% $FeO_T$ and 1–3 wt% MgO (see Supplementary Material II).

## 6. P–T conditions

The P–T crystallisation conditions of the studied lamproites were determined using the thermobarometric expressions established by Righter and Carmichael (1996). The thermometer and barometer consider the partition of $TiO_2$ and BaO between phlogopite-biotite and liquid in lamprophyres and lamproites. Fritschle et al. (2013) used this method to define the relative P–T trends between different lamproites from the Mediterranean area as well as between different types of phlogopites e.g., early-crystallised phenocryst and late-crystallised oikocryst. These authors noted that the method overestimates pressure and temperature because the $TiO_2$ and BaO contents in micas are strongly dependent on oxygen fugacity and phase association. In addition, the use of whole-rock rather than glass compositions may increase uncertainty. Furthermore, we used the geothermometer based on Al partitioning between olivine-spinel recalibrated by Wan et al. (2008) to cross-check the temperatures obtained in the type-A lamproite.

Taking into account the method limitations, we calculated the P–T conditions for the Socovos lamproites using only magma-derived phlogopites. We consider the $TiO_2$ and BaO whole-rock composition

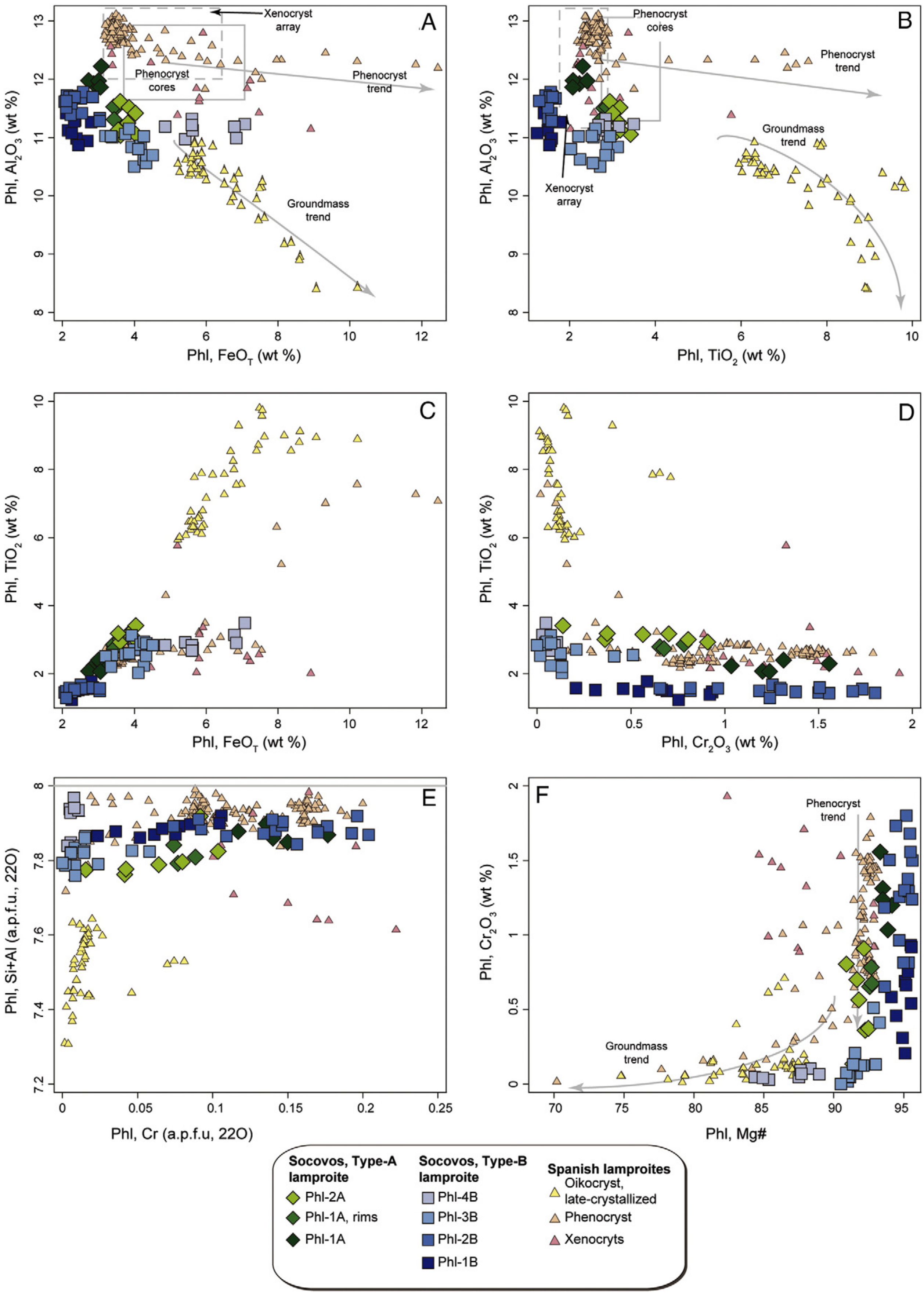


**Fig. 8.** Compositional variations of phlogopite from Socovos lamproites and Spanish lamproites (smaller and lighter symbols; data from Venturelli et al., 1984, 1988; Fritschle et al., 2013). A) $Al^2O^3$ vs $FeO^T$ and B) $Al^2O^3$ vs $TiO^2$, with indication of the xenocryst, phenocryst and groundmass arrays according to Fritschle et al., (2013). C) $TiO^2$ vs $FeO^T$. D) $TiO^2$ vs $Cr^2O^3$, E) Relationship between Si + Al vs Ti (atoms per 22 O); note that of phlogopites from Socovos lamproites have Si + Al < 8. F) $Cr^2O^3$ vs Mg#.

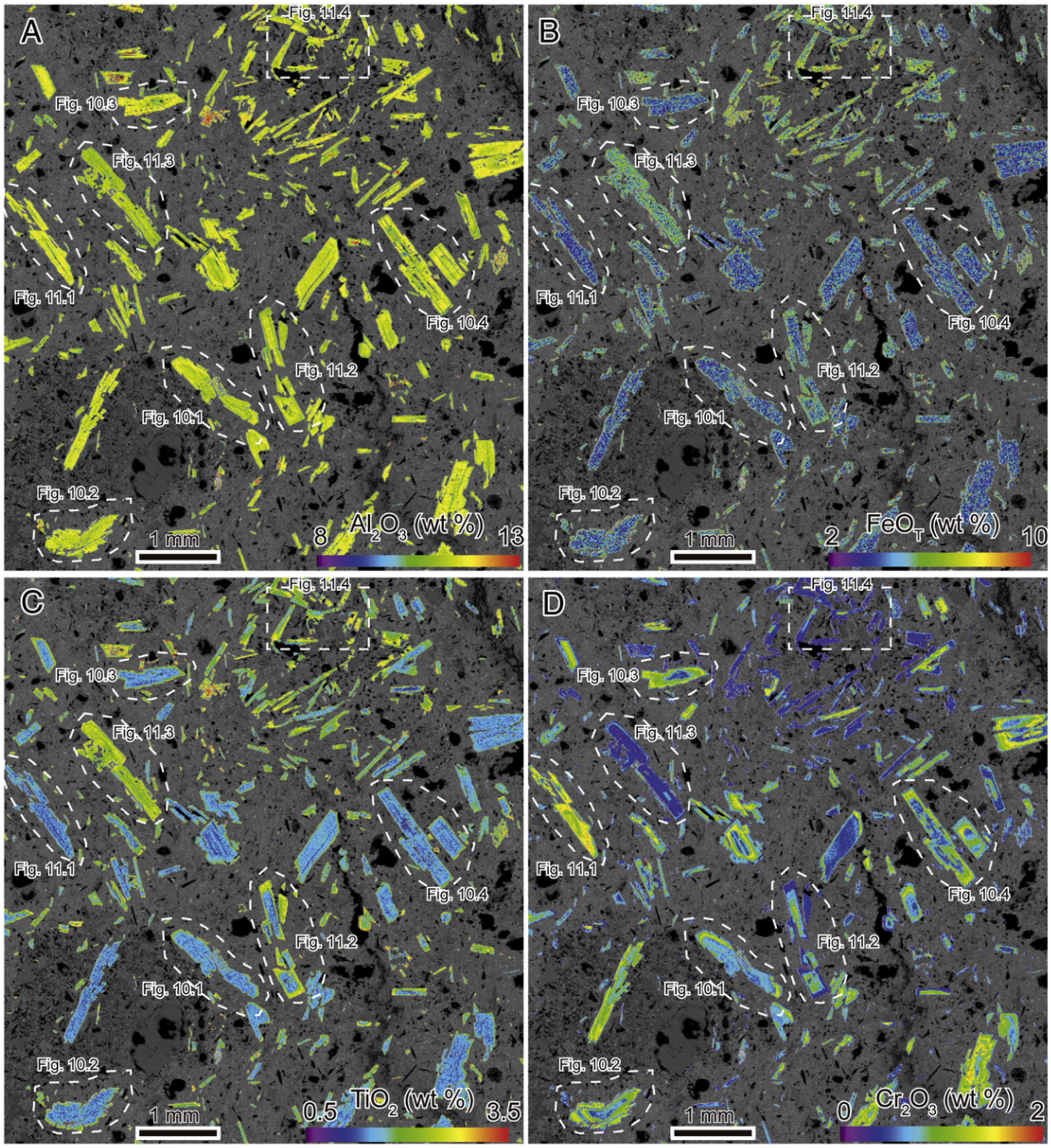


**Fig. 9.** Composite X-ray images of type-B lamproite. A) $Al_2O_3$ wt%, B) $FeO_T$ wt%, C) $TiO_2$ wt% and D) $Cr_2O_3$ wt%. The images are masked to show phlogopite set in a base layer of the corresponding backscattered electron image that shows the basic textural features of the scanned area. Representative examples of phlogopite types shown in Figs. 10 and 11 are indicated.

values of Pérez-Valera et al. (2013) to represent the liquid (cf., Fritschle et al., 2013). Thermobarometric estimations are given in Supplementary Material II. The calculated range of temperature and pressure determinations in both types of lamproites are 1116–1183 °C and 18–20 kbar (Fig. 13), within method errors of ± 50 °C and ± 4 kbar (cf., Righter and Carmichael, 1996). Groundmass Phl-4B from type-B lamproite gave lower pressure *c.* 13 kbar but a similar temperature *c.* 1108 °C (Fig. 13). Moreover, the temperatures obtained for the type-A lamproite fit with the temperature of olivine-spinel pairs, with a range of 1000–1275 °C (results in Supplementary Material II). The temperature determinations are consistent with the range of world-wide lamproite phlogopite crystallisation, whereas barometric calculations agree with estimations in other Spanish lamproites (Fig. 13; cf., Barton and Hamilton, 1982; Fritschle et al., 2013; Condamine and Médard, 2014).

## 7. Discussion

To decipher the role of magma mixing and storage at mantle depths in the observed mineralogical complexity of the Socovos lamproites we first characterise the magma from which they crystallised, the conditions of melting and crystallisation and the tectonomagmatic context. Having established these constraints the mantle source character, melting and subsequent magma interaction processes may be considered.

### 7.1. Lamproite magma characterisation

Based on current geochemical classifications (cf., Le Maitre, 2005; Mitchell and Bergman, 1991), the Socovos fault volcanic rocks can be characterised as primitive Si-rich (55–60 $SiO_2$ wt%) lamproites *ss* with a pristine mantle origin. They have the same compositions as typical NVP lamproites such as Calasparra, Cancarix and Jumilla (Fig. 1A). Their geochemical features significantly differ from other NVP ultrapotassic rocks, minettes, formed by interaction of lamproitic magmas and assimilation or mixing with continental crust (Supplementary Figs. S1 to S5; Venturelli et al., 1984, 1988, 1991; Toscani et al., 1995; Cambeses et al., 2013).

The mineral textures and chemistry of the studied samples also support the unmodified mantle-derived true lamproite character of Socovos volcanic rocks. According to the criteria of Mitchell and

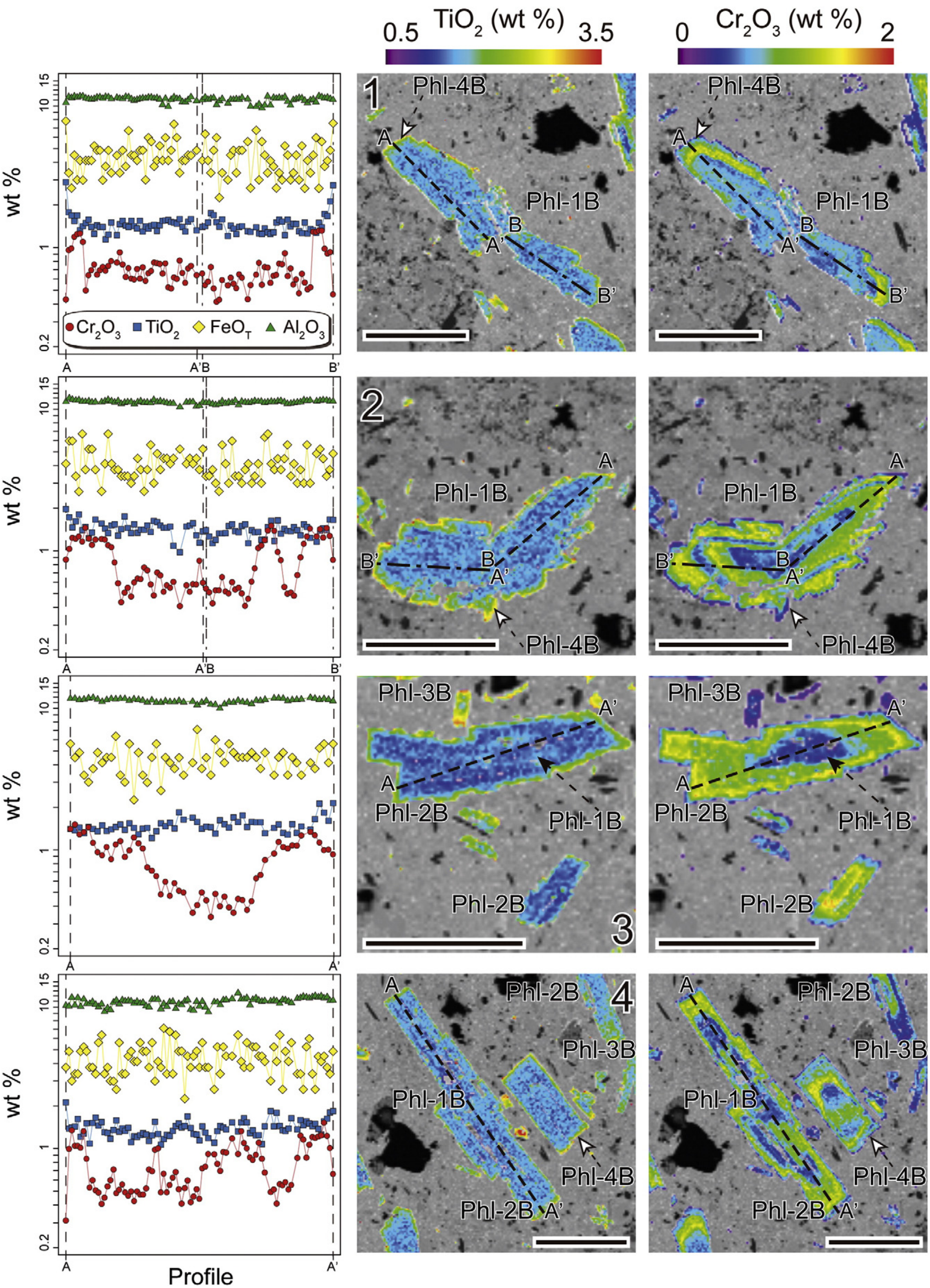


**Fig. 10.** Detailed composite X-ray images of $TiO_2$ wt% and $Cr_2O_3$ wt% of phlogopite types from type-B lamproite. Profiles show distribution of $Al_2O_3$ wt%, $FeO_T$ wt%, $TiO_2$ wt% and $Cr_2O_3$ wt% extracted from the quantified images. Phlogopite types Phl-1B, Phl-2B and Phl-3B are indicated. Scale bar: 500 μm.

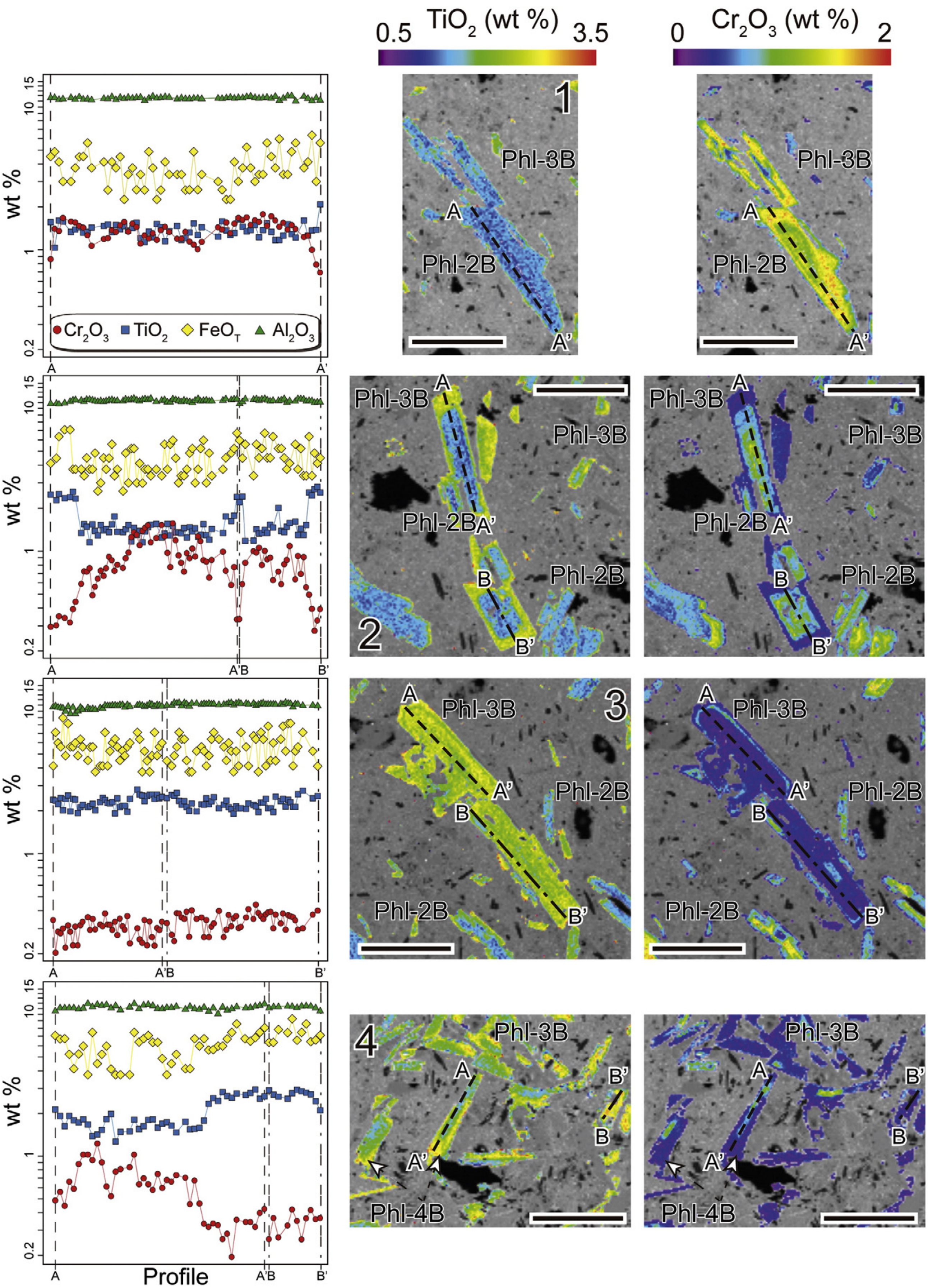


**Fig. 11.** Detailed composite X-ray images of $TiO^2$ wt% and $Cr^2O^3$ wt% of phlogopite types from type-B lamproite. Profiles show distribution of $Al^2O^3$ wt%, $FeO^T$ wt%, $TiO^2$ wt% and $Cr^2O^3$ wt% extracted from the quantified images. Phlogopite types Phl-2B, Phl-3B and Phl-4B are indicated. Scale bar: 500 μm.

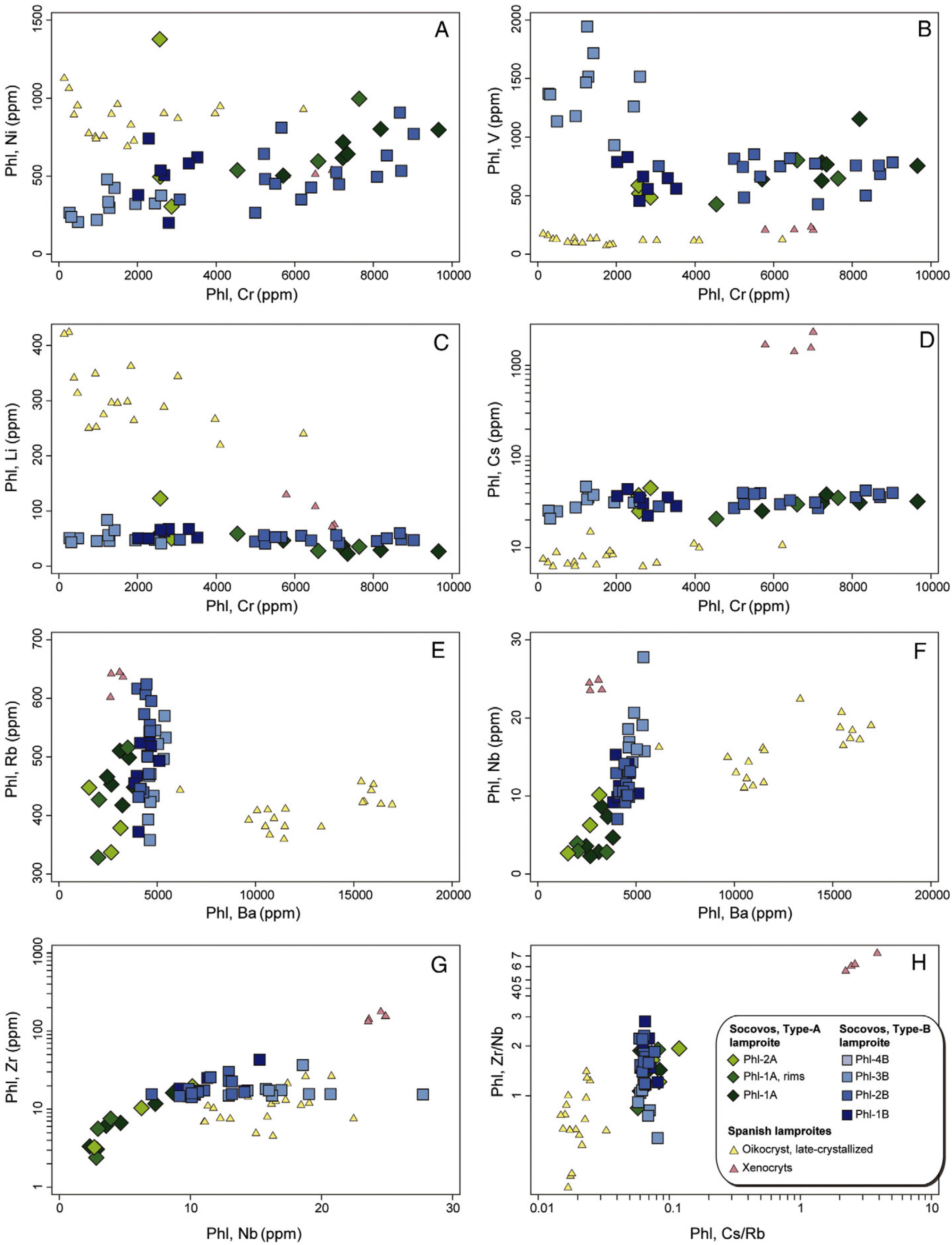


**Fig. 12.** Representative trace element variations in phlogopites from Socovos lamproites and Spanish lamproites (smaller and lighter symbols; data from Fritschle et al., 2013): A) Ni vs Cr. B) V vs Cr. C) Li vs Cr. D) Cs vs Cr. E) Rb vs Ba. F) Nb vs Ba. G) Zr vs Nb. H) Zr/Nb vs Cs/Rb.

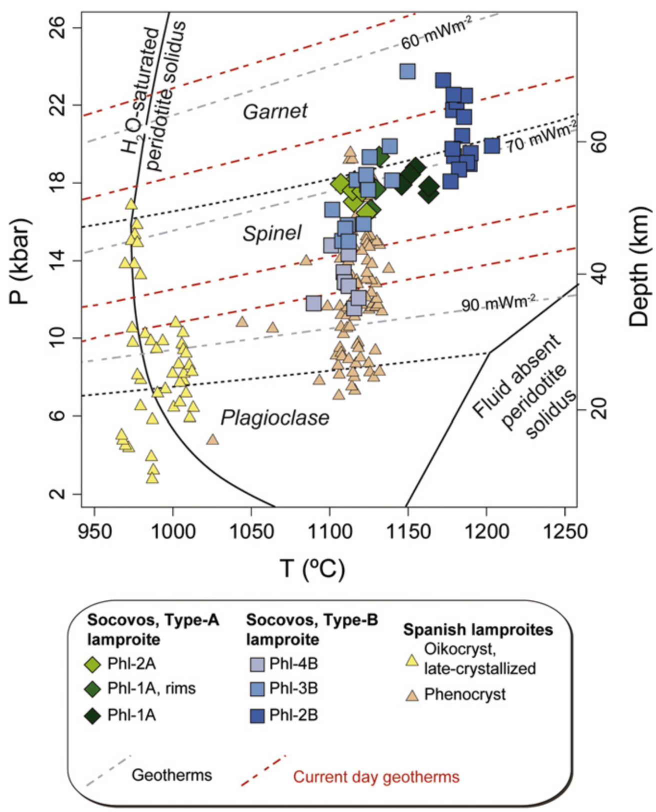


**Fig. 13.** Pressure and temperature estimations for melt-derived phlogopites from Socovos lamproites (see text for explanation) and thermobarometric estimation from Spanish lamproites (smaller and lighter symbols; data from Fritschle et al., 2013). The $H_2O$ saturated and fluid absent solidi of peridotite (solid lines) and the stability fields of garnet, spinel and plagioclase (dotted lines) are indicated (Kushiro and Yoder, 1966; Kushiro et al., 1968; O'Neil, 1981; Takahashi, 1986). The general grey-colour dashed geotherms (*c*. 60–90 mW $m^{-2}$) are Philpotts (1990) and the present day red-colour dashed geotherms beneath the Alboran Domain are from Soto et al. (2008).

Bergman (1991), the Socovos lamproites mineral compositions do not reflect magma–crust interaction, for example: i) forsterite olivine with Fo 90–94% (Fig. 4), ii) Al- and Ti-poor augite clinopyroxene (Fig. 6), iii) Al-poor and Mg-rich phlogopite (Fig. 8) and iv) Fe-rich sanidine. In this regard, it is notable that all types of micas in the studied samples are Si + Al-deficient relative to the tetrahedral sites, a distinctive feature of primitive lamproite mica (Fig. 8E).

### *7.2. P–T conditions of source region partial melting and subsequent crystallisation*

Although the lamproite magma was emplaced at upper crustal depths, P–T determinations on magma-derived phlogopite phenocrysts indicate the onset of crystallisation at 1100–1200 °C and 60–70 km depth (Fig. 13). These crystallisation conditions are similar to early-stage phenocrysts from other Spanish lamproites (Fig. 13). On the other hand, groundmass phlogopite, Phl-4B, from the type-B lamproite crystallised at a distinctly shallower depth of *c*. 45 km albeit at a comparable temperature *c*. 1100 °C, pointing to crystallisation as the magma ascended. However, lower pressure and temperature groundmass phlogopites (i.e., the oikocrysts of Fritschle et al., 2013) found in other Spanish lamproites are not detected in our samples (Fig. 13). The different crystallisation conditions of these late-stage phlogopites suggest their formation near or at the upper crustal emplacement level. So, phlogopites from the Socovos lamproites record successive crystallisation of the primitive lamproitic magma close the mantle source, far from the shallow crust.

The *c*. 60–70 km crystallisation depth determined here points to the subcontinental lithospheric mantle during the Miocene (e.g., Palomeras et al., 2014; Thurner et al., 2014). Prelević and Foley (2007) noted that petrological and geochemical features together with experimental results indicated, that the Spanish lamproite magmas were generated at relatively low pressure (30–60 km) similar to other Si-rich lamproites (cf., Condamine and Médard, 2014; Foley, 1989, 1993). Notably, the presence of mantle-derived spinel xenocrysts (Spl-1) in type-B lamproite supports the relatively low pressure, below the garnet stability field, Socovos fault lamproite magma generation. Then, the P–T range of early phlogopite phenocrysts obtained in present work indicates that the lamproite magmas started to crystallise soon after generation and segregation at subcontinental lithospheric mantle depths (Fig. 13). The P–T results record a sequence of partial melting, segregation, crystallisation and subsequent rapid adiabatic ascent consistent with emplacement in the fault system of a dynamic tectonic scenario.

### *7.3. Geodynamic setting of magma formation and ascent*

The geodynamic scenario associated with NVP lamproite magma generation in the Betic-Rif orogen can be conceptualised within three post-collisional orogenic models: i) subduction rollback (e.g., Gutscher et al., 2012; Lonergan and White, 1997; Rosenbaum and Lister, 2004; Royden, 1993); ii) continental delamination and/or convective removal of an over-thickened continental lithosphere (e.g., Mancilla et al., 2013; Turner et al., 1999), and iii) a combined rollback-delamination models (e.g., Do Couto et al., 2016; Mancilla et al., 2015; Palomeras et al., 2014).

In all the above models a subduction zone, active during Middle-Upper Miocene, formed the tholeiitic-calc-alkaline series of the NVP (e.g., Booth-Rea et al., 2007; Duggen et al., 2005, 2008; Hoernle et al., 1999). It has been suggested that complex rollback evolution of the subduction zone triggered slab tearing, which produced edge delamination under the Betic-Rif orogen (e.g., Booth-Rea et al., 2007; Duggen et al., 2005; Mancilla et al., 2015). As a result, regional uplift and subsequent extension and asthenosphere upwelling have taken place in the westernmost Mediterranean since the Late Miocene to the present day (e.g., Argles et al., 1999; Díaz et al., 2010; Pérez-Peña et al., 2010). An associated rise of the conductive geothermal gradient in the back-arc region resulted in partial melting of the extended continental crust and mantle from 12 Ma onwards (Álvarez-Valero and Kriegsman, 2007, 2008; Cesare et al., 2003, 2009; Duggen et al., 2005; Turner et al., 1999). These events are still detectable beneath the Alboran Domain (Soto et al., 2008).

The lamproites at Socovos and other localities of the NVP were generated in this context of regional uplift, extension and asthenosphere upwelling. Post-collisional strike-slip faults, likely rooted in the extended lithospheric mantle, formed a plumbing system through which lamproitic magmas ascended rapidly to upper crustal levels (cf., Vaughan and Scarrow, 2003). In the Socovos fault this process took place over a period of *c*. 2 million years (Pérez-Valera et al., 2013). The Socovos fault is not, however, an isolated structure, comparable strike-slip deformation is common throughout the Betic Cordillera (e.g., Barcos et al., 2015 and references therein). Similar deformation affected Betic subcontinental lithospheric mantle as observed in xenoliths from the nearby Tallante area (e.g., Konnc, 2013).

### *7.4. Heterogeneous lamproite mantle source*

Lamproite magmas are derived from refractory harzburgite mantle re-fertilised by metasomatism to produce mica-amphibole-bearing harzburgite and pyroxenite (e.g., Foley, 1989, 1990; Jaques et al., 1984; Mirnejad and Bell, 2006; Prelević et al., 2008). Residual harzburgite may result from melting and magma extraction in the mantle above a subduction zone. Metasomatism, on the other hand, is related to accretion of subducted sediments in the mantle and/or advection of sediment-derived fluids-melts (Prelević and Foley, 2007). Both, an ultradepleted source (Prelević and Foley, 2007; Prelević et al., 2010a, 2013) and a contribution of subducted-related material (e.g., Benito et al., 1999; Conticelli et al., 2009; Prelević et al., 2008) have been identified in NVP lamproites.

A contribution of subducted material in the NVP lamproites source, including those from the Socovos, is supported by whole-rock LILE enrichment relative to HFSE; high Pb; depletion in Ti, Nb and Ta; and Sr–Nd–Pb and Hf isotopes (e.g., Duggen et al., 2005; Prelević et al., 2008, 2010b; Conticelli et al., 2009 and Supplementary Figs. S1 to S5). Moreover, compositional variations in the main lamproite minerals, particularly trace elements, point to a subducted continent-derived sediment source component: high concentrations of Li, Zn and P in olivine phenocrysts, Ol-1, from type-A lamproite (Fig. 4); and high Li and Cs in phlogopites phenocrysts from both lamproite types (Fig. 12; cf., Fritschle et al., 2013; Prelević et al., 2013; Foley et al., 2013). In addition, phlogopites from the Socovos lamproites have high Zr/Nb (0.55–2.81) and Cs/Rb (0.05–0.11) (Fig. 12H). This is significantly different from other phlogopites from the nearby Jumilla lamproites (Fig. 12H). Fritschle et al. (2013) attributed these characteristics to heterogeneous metasomatism of the mantle source.

In the Socovos fault lamproites, an ultradepleted source is indicated by type-A lamproite olivine. Olivine comprises both mantle xenocrysts (anhedral and deformed Ol-1 grains) and phenocrysts (Ol-2). The phenocrysts and xenocryst overgrowth rims have distinct enrichment in Fo, Ni, Ca, Cr, Li and P (Figs. 4 and 5). Prelević and Foley (2007) related extreme Fo contents in olivine phenocrysts with crystallisation from a high-Si and low-Mg alkaline melt. Such melts have high Ni, Zn and Cr olivine-melt distribution coefficients ($D^{olivine/melt}$) which explains the higher concentration of these elements in phenocryst rather than xenocryst (Fig. 4). Comparable compositional relationships are also recognised in olivines, xenocryst and phenocrysts, from other NVP lamproites (Fig. 4; Venturelli et al., 1984; Prelević and Foley, 2007; Prelević et al., 2013). So, the extreme Fo contents and chromite inclusions with particularly high Cr# of the Socovos lamproites (Fig. 4D) support a refractory hazburgite mantle source composition (cf., Foley, 1992a; Prelević and Foley, 2007; Prelević et al., 2010a, 2013).

However, the olivine-lacking type-B lamproite cannot be related to a metasomatised depleted harzburgite source, instead, a fertile pyroxenite source seems more plausible. Foley (1992b) proposed a model in which K-rich (amphibole- and phlogopite-bearing) pyroxenite veins are formed during mantle re-enrichment. In addition, experimental studies of Si-rich lamproites highlight the absence of olivine as liquidus phase over a wide range of pressures, indicating a pyroxenite source (Foley, 1989, 1992b; Mitchell, 1995; Mitchell and Edgar, 2002). The suggestion of a fertile mantle source for the type-B lamproites is strengthened by the presence of the spinel xenocrysts, Spl-1, with lower Cr# $\approx$ 0.22–0.23. Furthermore, localised oscillatory zoning in phlogopite xenocrysts, Phl-1B (Fig. 10.2) indicates an open system during crystallisation which may be attributed to source metasomatism (cf., Foley, 1992a). We thus propose that the Socovos fault lamproites record melting of both metasomatised harzburgite and veined-pyroxenite sources. The close surface proximity of the two lamproite types implies that the mantle source region was heterogeneous (cf., Prelević and Foley, 2007; Prelević et al., 2008, 2010b).

Notably, the olivine-lacking type-B lamproite predates, by *c.* 2 Ma, the Ol-bearing type-A lamproite both at Socovos and elsewhere in the NVP, such as Cancarix (*c.* 9.3 Ma vs. 7.2–7.0 Ma; Duggen et al., 2005; Pérez-Valera et al., 2013). This points towards progression from melting of a more fertile pyroxenite source to more extended melting of a refractory harzburgite source. This scenario fits with a rise of the conductive geothermal gradient triggered by lithospheric extension and asthenosphere upwelling.

### 7.5. Lamproite magma mixing at mantle depths

A heterogeneous mantle source was tapped by at Socovos, this gave rise to distinct batches of lamproitic magma that mingled-mixed at mantle depths. These processes are clearly indicated by significant differences in the composition and zoning of phenocrysts.

#### 7.5.1. Mineralogical evidence of magma mixing processes

The presence of xenocryst, phenocryst and groundmass minerals in the Socovos lamproites clearly point to a varied origin. The phenocrysts, in particular, are texturally and compositionally diverse. Recognition of distinct magma-derived crystals in a single sample, e.g., the type-B lamproite, suggests that they precipitated from more than one magma.

Late-stage groundmass clinopyroxene in the type-A lamproite reveals that crystallisation resulted in progressive depletion in Mg# and Cr and enrichment in Ti (Figs. 6 and 7). This compositional variation is also observed in late-stage clinopyroxene from other NVP lamproites (Contini et al., 1993; López-Ruiz and Rodriguez-Badiola, 1980; Venturelli et al., 1984, 1988).

Type-B lamproite clinopyroxenes have a more complex history. Two types of phenocrysts with different Cr and Ti contents are recognisable: Cpx-1, Cr- and Ti-poor, which includes phlogopite phenocryst Phl-3B (Figs. 3A, 6 and 7), and Cpx-3, Cr- and Ti-rich (Figs. 3B, 6 and 7). These two types of phenocrysts indicate early crystallisation from different primitive lamproite magmas, the Mg# of both Cpx-1 and -3 is high (Fig. 6). After crystallisation both types reequilibrated, Cpx-2 and the rims of Cpx-3 then crystallised with intermediate compositions in terms of Cr and Ti (Figs. 6 and 7). These mineral chemistry relationships indicate different magmatic sources for Cpx-1 and Cpx-3 and hence that magma mixing occurred at an early stage of evolution of type-B lamproite.

In the analysis of the phlogopites we follow the classification of Fritschle et al. (2013), who established xenocryst, phenocryst and groundmass compositional arrays based on $Al_2O_3$, $FeO_T$ and $TiO_2$ variations (cf., Mitchell and Bergman, 1991). Phlogopites from Socovos lamproites fit their xenocryst and phenocryst arrays (Fig. 8A and B).

All type-A lamproite phlogopites are magma-derived. Their high Mg# (90–94) and restricted $TiO_2$ and $FeO_T$ and high $Al_2O_3$ contents reflect less evolved differentiation trend (Fig. 8). Even the most evolved phlogopite Phl-2A do not overlap with late-stage Fe- and Ti-rich and Mg#-poor phenocryst and groundmass including oikocrysts from other NVP lamproites (Fig. 8). This indicates that all type-A lamproite phlogopites are early-stage. Furthermore, Fo- (88–85%), Ni- and Cr-poor magmatic olivine crystallised after more extensive magma fractionation (Prelević and Foley, 2007; Prelević et al., 2013; Venturelli et al., 1984) is absent in Socovos lamproites (Fig. 4), strengthening a near-primitive magma nature of the type-A lamproite and the lack of significant fractionation.

Notably, Phl-1A phlogopites have higher Cr contents than other more evolved micas (Fig. 8). These higher Cr contents correlate with other trace elements, such as Ni (Fig. 12) in agreement with type-A Cr- and Ni-rich olivine phenocrysts Ol-2 (Fig. 4). Although high Cr content in phlogopite is commonly associated with mantle-derived xenocrysts (e.g., Fritschle et al., 2013; Prelević et al., 2010a), the type-A lamproite phlogopites have no reabsorbed rims or other disequilibrium texture (Fig. 2C). Therefore, high Cr phlogopites may also have formed as early-stage crystallisation phenocrysts.

The type-B Phl-1B phlogopites have kinked textures (Figs. 3C and 9) characteristic of mantle-derived xenocrysts *ss*. These xenocrysts were subsequently resorbed and overgrown by reequilibrated rims with a composition similar to magma-derived Phl-2B (Fig. 10.3 and 10.4). Some compositional characteristics of Phl-2B megacrysts and medium-small phenocrysts are similar to the Phl-1B xenocrysts: low Ti, Fe and high Mg# (Fig. 8). However, phlogopite Phl-2B has distinctively higher Cr content (Figs. 8, 9, 10 and 11) in the range of Phl-1A phenocrysts from the type-A lamproite (Fig. 8).

Significantly, phlogopite Phl-2B has sharp compositional boundaries with Phl-3B overgrowth rims (Figs. 9 and 11.2). The compositions of Phl-2B and Phl-3B are different, in particular for Ti and Cr (Fig. 11.1 and 11.3). In addition, Phl-3B are present as inclusions in Cpx-1 phenocrysts (Fig. 3A). Both are Cr-poor early crystallisation phases (Figs. 6 and 8), from a Cr-poor lamproite magma. By contrast, Phl-2B are Cr-rich like the Cpx-3 phenocryst. These contrasted mineral assemblages indicate that they crystallised from different lamproite magmas. Other trace elements compositions also highlight the differences between Phl-2B and Phl-3B micas, e.g., Ni and V (Fig. 12). Furthermore, the high HFSE content in Phl-3B relative to Phl-2B is anomalous for micas (cf., Schmidt et al., 1999). We suggest that the high HFSE derived from melting of an ilmenite + rutile-bearing pyroxenite vein source (cf., Fritschle et al., 2013; Lorand and Gregoire, 2010). The textural and compositional interrelationships between the Phl-2B and Phl-3B phlogopites reveal the role of mingling-mixing processes during the early stage of evolution of the type-B lamproites.

*7.5.2. Model of magma mixing at mantle depths*

Mixing processes of metasomatic pyroxenite vein-derived and wall-rock peridotite-derived melts or of melts derived from heterogeneous veins have been proposed for ultrapotassic magmas (e.g., Azzone

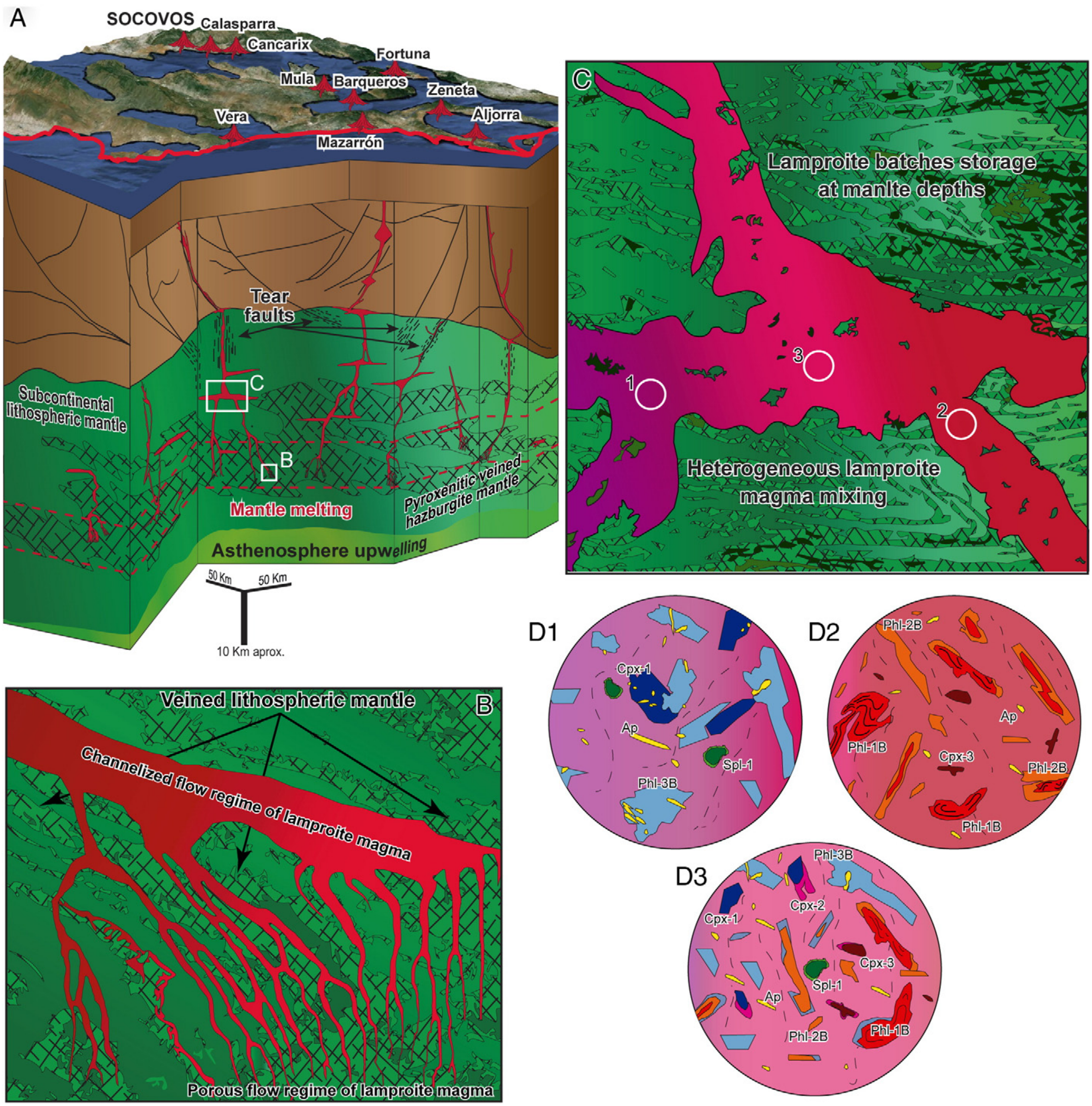


**Fig. 14.** Schematic model of veined metasomatised mantle beneath the Betic Cordillera at *c.* 9 Ma. Palaeogeographic reconstruction based on Cambeses and Scarrow (2013). Red solid line represents current coast line. Ultrapotassic occurrences are indicated. Mantle partial melting occurred at 60–70 km depth. Lamproite magmas propagated along fractures swarm upwards through lithosphere, with lateral spread after progressive crystallisation. B) Detail of the beginning of melting of pyroxenitic veined mantle from porous to channelised flow regimes, when mobilisation is controlled by magma-filled fractures. C) Scheme for coalescence of heterogeneous lamproite magma and storage and mixing of magma batches at mantle depths. Circles 1 to 3 are sketches of varied lamproite magma-derived phases and magma mixing process.

et al., 2013; Conticelli et al., 2011). Compositional relationships of early crystallised minerals, such as olivine and clinopyroxene, have been used to suggest mixing of heterogeneous mantle-derived melts in magma chambers-reservoirs at the upper mantle and crust–mantle boundary (Semiz et al., 2012; Ubide et al., 2014a, 2014b; Xu et al., 2003). In the Socovos pyroxenite vein-derived type-B lamproites the primitive character and complex deep-seated crystallisation of the main minerals i.e., clinopyroxene and phlogopite evidence magma mixing. Batches of ultrapotassic magma were extracted from their sources and commenced crystallisation and mixing at mantle depths.

In this context, we suggest that a relatively high melt fraction in pyroxenite veins favoured magma transport from the source by means of initial porous flow that progressed to channelised flow in a heterogeneous mantle melting zone (Fig. 14A and B; Spera, 1987; Kelemen et al., 1995; Halvin et al., 2013; Miller et al., 2014). The vein-derived high-melt fraction magma propagated as swarm of dykes in fractures upwards through the lithosphere. Their ascent was facilitated by: the lower density of the magma compared to the solid host rock; the low viscosity of the lamproite magma; and the overpressure imposed by the relatively high volatile content of the lamproite magma (Fig. 14A and B; cf., Mitchell and Bergman, 1991). Magma crystallisation during ascent slowed the upward progression of dyke propagation. This resulted in the lateral spread of fractures and horizontal layer formation in because of gravitational and compaction constraints (Fig. 14A and C; cf., Foley, 1992b). Channelised flow, formation of reservoirs and partial storage of lamproite magmas batches derived from heterogeneous sources clearly favour mixing (Fig. 14C; cf., Katz and Weatherley, 2012). These processes were interrupted when the Socovos fault penetrated through the crust to the mantle reaching the magma chambers-reservoirs, triggering rapid ascent of the heterogeneous lamproite magma (Fig. 14A).

We propose that the type-B lamproite formed after mixing at mantle depths (60–70 km) of, at least, two magma batches from a heterogeneous source (Fig. 14D1 to D3). One of the magmas was Cr-rich phlogopite- and clinopyroxene-bearing whereas the other contained Cr-poor phlogopite and clinopyroxene phenocrysts (Fig. 14D1 to D3). The type-A lamproite, on the other hand, apparently represents a single batch of magma derived from an olivine pyroxene-bearing harzburgite source that was only affected by minor fractionation processes. The latter is the typical lamproite of the region e.g., Jumilla and Cancarix (Mitchell and Bergman, 1991). By contrast, magma mixing at depth as reflected in the type-B lamproite is apparently scarce or it has not previously been detected. In this regard the combined textural and compositional information provided by X-ray maps of the mineral assemblage has proven critical in detecting and interpreting the complex mantle mixing and crystallisation processes recorded in the Socovos fault lamproites.

## 8. Conclusions

The Socovos fault lamproites (SE Spain Neogene Volcanic Province) represent a direct window to observe complex petrogenetic mingling-mixing processes and magma batch storage at mantle depths. The detailed textural and compositional study of Socovos fault lamproites petrogenetic minerals clearly point to varied origins; i) crystals incorporated from varied mantle rocks, xenocrysts; and ii) precipitated at an early stage, phenocrysts, from distinct lamproite magmas.

The Socovos fault zone rocks represent primitive lamproite magmas s.s. Our calculated P–T crystallisation conditions were 1100–1200 °C at 60–70 km depth in a spinel-bearing subcontinental lithospheric mantle. The petrogenetic minerals indicate that the mantle source was a heterogeneous harzburgite-pyroxenite metasomatised during the influx of subduction-derived melts-fluids. The melting process was triggered by extension, asthenosphere upwelling and associated rise of the conductive geothermal gradient in the back-arc region of the westernmost Mediterranean since the Late Miocene until present.

The heterogeneous mantle source melting produced distinct magma batches; metasomatised harzburgite- and pyroxenite vein-derived. Both types of magmas are preserved in the Socovos fault lamproites, defined here as type-A and type B lamproites respectively. The Ol-lacking type-B predates Ol-bearing type-A by *c.* 2 million years. We propose that mantle partial melting preferentially affected metasomatised pyroxenite veins in a scenario of increasing geothermal gradient. Upon progressive heating, magmas from metasomatised, albeit more refractory, harzburgite dominated the melting zone. We suggest that these heterogeneous magmas were channelled as a swarm of dykes in fractures upward through the mantle and were stored in chambers-reservoirs at mantle depths. There they partly crystallised and eventually mixed with advecting magma batches.

The variety of petrogenetic minerals studied in the present work evidence the interaction and mingling-mixing of ultrapotassic magma batches at mantle depths. This process was interrupted when the lithospheric-scale Socovos fault reached and tapped the magma chambers-reservoirs triggering rapid ascent of lamproite magma.

The combined textural and compositional information provided by X-ray maps has proven critical in the interpretation of the complex evolution of the Socovos fault lamproites. It allowed quantification of mineral chemistry permitting identification of compositional variations including zoning and also the textural positions of key minerals. This approach may be applied to decipher as yet unidentified mineral features by extensive imaging of extended sample sets in this and other locations.

Supplementary data to this article can be found online at doi:10.1016/j.lithos.2016.10.006.

## Acknowledgements

We thank one anonymous reviewer and Dejan Prelević for the thorough revision of the manuscript and for their insightful comments. Nelson Eby is thanked for his editorial handling and constructive comments. This study has been financially supported by the Andalusian grant RNM2163 and the Spanish grants CGL2008-02864 and CGL2013-40785-P. We also appreciate financial support of a *Plan Propio* grant from the University of Granada Vicerrectorate of Research and Transfer.

## References

Álvarez-Valero, A.M., Kriegsman, L.M., 2007. Crustal thinning and mafic underplating beneath the Neogene Volcanic Province (Betic Cordillera, SE Spain): evidence from crustal xenoliths. Terra Nova 19, 266–271.

Álvarez-Valero, A.M., Kriegsman, L.M., 2008. Partial crustal melting beneath the Betic Cordillera (SE Spain): the case study of Mar Menor volcanic suite. Lithos 101, 379–396.

Argles, T.W., Platt, J.P., Waters, D.J., 1999. Attenuation and excision of a crustal section during extensional exhumation: the Carratraca Massif, Betic Cordillera, Southern Spain. Journal of the Geological Society of London 156, 149–162.

Arima, M., Edgar, A.D., 1983. High pressure experimental studies of a katungite and their bearing on the genesis of some potassium-rich magmas of the West Branch of the African Rift. Journal of Petrology 24, 166–187.

Azzone, R.G., Enrich, G.E.R., de Barros-Gomes, C., Ruberti, E., 2013. Trace element composition of parental magmas from maficeultramafic cumulates determined by in situ mineral analyses: the Juquiá maficeultramafic alkalineecarbonatite massif, SE Brazil. Journal of South American Earth Sciences 41, 5–21.

Barcos, L., Balanyá, J.C., Díaz-Azpiroz, M., Expósito, I., Jiménez-Bonilla, A., 2015. Kinematics of the Torcal Shear Zone: transpressional tectonics in a salient-recess transition at the northern Gibraltar Arc. Tectonophysics 663, 62–77.

Barton, M., Hamilton, D.L., 1982. Water-saturated melting experiments bearing upon the origin of potassium-rich magmas. Mineralogical Magazine 45, 267–278.

Barton, M., Varekamp, J.C., van Bergen, M.J., 1982. Complex zoning of clinopyroxenes in the lavas of Vulsini, Latium, Italy: evidence for magma mixing. Journal of Volcanology and Geothermal Research 14, 361–388.

Bellon, H., Bordet, P., Moutenat, G., 1983. Chronique de magmatisme neogene des cordilleres bétiques (Espagne Meridionale). Bulletin de la Société Géologique de France 25, 205–217.

Benito, R., López-Ruiz, J., Cebriá, J.M., Hertogen, J., Doblas, M., Oyarzun, R., Demaiffe, D., 1999. Sr and O isotope constraints on source and crustal contamination in the high-K calc-alkaline and shoshonitic neogene volcanic rocks of SE Spain. Lithos 46 (4), 773–802.

Booth-Rea, G., Ranero, C.R., Martínez-Martínez, J.M., Grevemeyer, I., 2007. Crustal types and Tertiary tectonic evolution of the Alborán sea, western Mediterranean. Geochemistry, Geophysics, Geosystems 8 (10), Q10005.

Cambeses, A., Scarrow, J.H., 2013. Ultrapotassic volcanic centres as potential paleogeographic indicators: the Mediterranean Tortonian 'salinity crisis', southern Spain. Geologica Acta 11, 295–310.

Cambeses, A., García-Casco, A., Scarrow, J.H., 2013. Magmas mantélicos a través de un complejo anatéctico: evidencias texturales y composicionales de micas en lamproitas de la región Neógena volcánica del sureste de España. Geogaceta 54, 55–58.

Cesare, B., Gomez-Pugnaire, M.T., Rubatto, D., 2003. Residence time of S-type anatectic magmas beneath the Neogene Volcanic Province of SE Spain: a zircon and monazite SHRIMP study. Contributions to Mineralogy and Petrology 146, 28–43.

Cesare, B., Rubatto, D., Gómez-Pugnaire, M.T., 2009. Do extrusion ages reflect magma generation processes at depth? An example from the Neogene Volcanic Province of SE Spain. Contributions to Mineralogy and Petrology 157, 267–279.

Comas, M.C., Platt, J.P., Soto, J.I., Watts, A.B., 1999. The origin and tectonic history of the Alboran Basin: insights from Leg 161 results. Proceeding of the Ocean Drilling Program, Scientific Results 161, 555–580.

Condamine, P., Médard, E., 2014. Experimental melting of phlogopite-bearing mantle at 1 GPa: implications for potassic magmatism. Earth and Planetary Science Letters 397, 80–92.

Conticelli, S., Guarnieri, L., Farinelli, A., Mattei, M., Avanzinelli, R., Bianchini, G., Boari, E., Tommasini, S., Tiepolo, M., Prelević, D., Venturelli, G., 2009. Trace elements and Sr–Nd–Pb isotopes of K-rich, shoshonitic, and calc-alkaline magmatism of the western Mediterranean region: genesis of ultrapotassic to calc-alkaline magmatic associations in a post-collisional geodynamic setting. Lithos 107, 68–92.

Conticelli, S., Avanzinelli, R., Marchionni, S., Tommasini, S., Melluso, L., 2011. Sr–Nd–Pb isotopes from the Radicofani Volcano, Central Italy: constraints on heterogeneities in a veined mantle responsible for the shift from ultrapotassic shoshonite to basaltic andesite magmas in a post-collisional setting. Mineralogy and Petrology 103, 123–148.

Contini, S., Venturelli, G., Toscani, L., 1993. Cr–Zr-armalcolite-bearing lamproites of Cancarix, SE Spain. Mineralogical Magazine 57, 203–216.

Cvetković, V., Šarić, K., Prelević, D., Genser, J., Neubauer, F., Höck, V., van Quadt, A., 2013. An anorogenic pulse in a typical orogenic setting: the geochemical and geochronological record in the East Serbian latest Cretaceous to Palaeocene alkaline rocks. Lithos 180, 181–199.

Davidson, J.P., Morgan, D.J., Charlier, B.L.A., Harlou, R., Hora, J.M., 2007. Microsampling and isotopic analysis of igneous rocks: implications for the study of magmatic systems. Annual Review of Earth and Planetary Sciences 35, 273–311.

Díaz, J., Gallart, J., Villaseñor, A., Mancilla, F., Pazoz, A., Córdoba, D., Pulgar, J.A., Ibarra, P., Harnafi, M., 2010. Mantle dynamics beneath the Gibraltar Arc (western Mediterranean) from shear-wave splitting measurements on a dense seismic array. Geophysical Research Letters 37, L18304.

Do Couto, D., Gorini, C., Jolivert, L., Lbret, N., Augier, R., Gumiaux, C., d'Acremont, E., Ammar, A., Jabour, H., Auxietre, J.-L., 2016. Tectonic and stratigraphic evolution of the Western Alboran Sea Basin in the last 25 Myrs. Tectonophysics 667-678, 280–311.

Dobosi, G., Fodor, R.V., 1992. Magma fractionation, replenishment, and mixing as inferred from green-core clinopyroxenes in Pliocene basanite, southern Slovakia. Lithos 28, 133–150.

Duggen, S., Hoernle, K., Van Den Bogaard, P., Garbe-Schonberg, D., 2005. Post-collisional transition from subduction- to Intraplate-type magmatism in the Westernmost Mediterranean: evidence for continental-edge delamination of subcontinental lithosphere. Journal of Petrology 46, 1155–1201.

Duggen, S., Hoernle, K., Klügel, A., Geldmacher, J., Thirlwall, M., Hauff, F., Lowry, D., Oates, N., 2008. Geochemical zonation of the Miocene Alborán Basin volcanism (westernmost Mediterranean): geodynamic implications. Contributions to Mineralogy and Petrology 156 (5), 577–593.

Foley, S.F., 1989. Experimental constraints of phlogopite chemistry in lamproites: 1. The effect of water activity and oxygen fugacity. European Journal of Mineralogy 1, 411–426.

Foley, S.F., 1990. A review and assessment of experiments on kimberlites, lamproites and lamprophyres as a guide to their origin. Proceedings of the Indian Academy of Sciences - Earth and Planetary Sciences 99 (1), 57–80.

Foley, S.F., 1992a. Petrological characterization of the source components of potassic magmas: geochemical and experimental constraints. Lithos 28, 187–204.

Foley, S.F., 1992b. Vein-plus-wall-rock melting mechanisms in the lithosphere and the origin of potassic alkaline magmas. Lithos 28, 435–453.

Foley, S.F., 1993. An experimental study of olivine lamproite-first results from the diamond stability field. Geochimica et Cosmochimica Acta 57, 483–489.

Foley, S.F., Taylor, W.R., Green, D.H., 1986. The role of fluorine and oxygen fugacity in the genesis of the ultrapotassic rocks. Contributions to Mineralogy and Petrology 94, 183–192.

Foley, S.F., Prelević, D., Rehfeldt, T., Jacob, D.E., 2013. Minor and trace elements in olivines as probes into early igneous and mantle melting processes. Earth and Planetary Science Letters 363, 181–191.

Fritschle, T., Prelević, D., Foley, S.F., Jacob, D.E., 2013. Petrological characterization of the mantle source of Mediterranean lamproites: indications from major and trace elements of phlogopite. Chemical Geology 353, 267–279.

Fuster, J.M., 1967. Las rocas lamproiticas del SE de España. Estudios Geológicos 23, 3–69.

García-Hernández, M., López-Garrido, A.C., Rivas, P., Sanz de Galdeano, C., Vera, J.A., 1980. Mesozoic palaeogeographic evolution of the external zones of the Betic Cordillera. Geologie en Mijnbouw 50, 155–168.

Gernon, T.M., Spence, S., Trueman, C.N., Taylor, R.N., Rohling, E., Hatter, J.S., Harding, I.C., 2015. Emplacement of the Cabezo Mar'ıa lamproite volcano (Miocene, SE Spain). Bulletin of Volcanology 77. http://dx.doi.org/10.1007/s00445-015-0934-y.

Griffin, W.L., Wang, X., Jackson, S.E., Pearson, N.J., O'Reilly, S.Y., Xu, X., Zhou, X., 2002. Zircon chemistry and magma mixing, SE China: in-situ analysis of Hf isotopes, Tonglu and Pingtan igneous complexes. Lithos 61, 237–269.

Grützner, T., Prelević, D., Akal, C., 2013. Geochemistry and origin of ultramafic enclaves and their basanitic host rock from Kula Volcano, Turkey. Lithos 180–181, 58–73.

Gutscher, M.-A., Dominguez, S., Westbrook, G.K., Le Roy, P., Rosas, F., Duarte, J.C., Terrinha, P., Miranda, J.M., Graindorge, D., Gailler, A., Sallares, V., Bartolome, R., 2012. The Gibraltar subduction: a decade of new geophysical data. Tectonophysics 574–575, 72–91.

Halvin, C., Parmentier, E.M., Hirth, G., 2013. Dike propagation driven by melt accumulation at the lithosphere-asthenosphere boundary. Earth and Planetary Science Letters 376, 20–28.

Hoernle, K., van den Bogaard, P., Duggen, S., Mocek, B., Garbe-Schönberg, D., 1999. Evidence for Miocene subduction beneath the Alboran Sea: $^{40}Ar/^{39}Ar$ dating and geochemistry of volcanic rocks from Holes 977 A and 978 A. In: Zahn, R., Comas, M.C., Klaus, A. (Eds.), Proceedings of the Ocean Drilling Program, Scientific Results, 161. Ocean Drilling Program, College Station, TX, pp. 357–373.

Jaques, A.L., Lewis, J.D., Gregory, G.P., Ferguson, J., Smith, C.B., Chappell, B.W., McCulloch, M.T., 1984. The diamond-bearing ultrapotassic (lamproitic) rocks of the West Kimberley region, Western Australia. In: Kornprobst, J. (Ed.), Kimberlites and Related Rocks: Developments in Petrology, 9. Elsevier, Amsterdam, pp. 225–255.

Katz, R.F., Weatherley, S.M., 2012. Consequences of mantle heterogeneity for melt extraction at mid-ocean ridges. Earth and Planetary Science Letters 335-336, 226–237.

Kelemen, P.B., Shimizu, N., Salters, V.J.M., 1995. Extraction of mid-ocean-ridge basalt from upwelling mantle by focused flow of melt in dunite channels. Nature 375, 747–753.

Konnc, Z., 2013. Structure and Composition of the Subcontinetal Lithospheric Mantle in Convergent Setting: Insights from Mantle Xenoliths Hosted in Alkaline Magmatism Ph.D. thesis University of Granada-Conseji Superior de Investigaciones Científicas, Granada (226 pp.).

Kuiper, K.F., Krijgsman, W., Garcés, M., Wijbrans, J.R., 2006. Revised isotopic ($^{40}Ar/^{39}Ar$) age for the lamproite volcano of Cabezos Negros, Fortuna Basin (Eastern Betics, SE Spain). Palaeogeography, Palaeoclimatology, Palaeoecology 238 (1–4), 53–63.

Kushiro, I., Yoder, H.R., 1966. Anorthite-forsterite and anorthite-enstatie regions and their bearing on the basalt-eclogite transformation. Journal of Petrology 7, 337–362.

Kushiro, I., Syono, Y., Akimoto, S., 1968. Melting of a peridotite nodule at high pressure and high water pressures. Journal of Reophysical Research 73, 6023–6029.

Larsen, L.M., Pedersen, A.K., 2000. Processes in high-Mg, high-T magmas: evidence from olivine, chromite and glass in Paleogene Picrites from West Greenland. Journal of Petrology 41, 1071–1098.

Le Maitre, R.W., 2005. Igneous rocks: a classification and glossary of terms. Recommendations of the International Union of Geological Sciences Subcommission on the Systematics of Igneous Rocks, 2nd edition University Press, Cambridge (256 pp.).

Lonergan, L., White, N., 1997. Origin of the Betic-Rif mountain belt. Tectonics 16, 504–522.

López-Ruiz, J., Rodriguez-Badiola, E., 1980. La región volcanica neogena del sureste de España. Estudios Geológicos 36, 5–36.

Lorand, J.-P., Gregoire, M., 2010. Petrogenesis of Fe–Ti oxides in amphibole-rich veins from the Lherz orogenic peridotite (Northeastern Pyrénées, France). Contributions to Mineralogy and Petrology 160, 99–113.

Mancilla, F., Stich, D., Berrocoso, M., Martin, R., Morales, J., Fernandez-Ros, A., Paéz, R., Pérez-Peña, A., 2013. Delamination in the Betic Range: deep structure, seismicity and GPS motion. Geology 41, 307–310.

Mancilla, F., Booth-Rea, G., Stich, D., Pérez-Peña, J.V., Morales, J., Azañón, J.M., Matin, R., Giaconia, F., 2015. Tectonophysics 663, 225–237.

Miller, K.J., Zhu, W.-L., Montési, L.G.J., Gaetani, G.A., 2014. Experimental quantification of permeability of partially molten mantle rock. Earth and Planetary Science Letters 388, 273–282.

Mirnejad, H., Bell, K., 2006. Origin and source evolution of the Leucite Hills lamproites: evidence from Sr–Nd–Pb–O isotopic compositions. Journal of Petrology 47 (12), 2463–2489.

Mitchell, R.H., 1995. Melting experiments on a sanidine phlogopite lamproite at 4–7 GPa and their bearing on the sources of lamproitic magmas. Journal of Petrology 36 (5), 1455–1474.

Mitchell, R.H., 2008. Petrology of hypabyssal kimberlites: relevance to primary magma compositions. Journal of Volcanology and Geothermal Research 174, 1–8.

Mitchell, R.H., Bergman, S.C., 1991. Petrology of Lamproites. Plenum Press, New York (441 pp.).

Mitchell, R.H., Edgar, A.D., 2002. Melting experiments on $SiO_2$-rich lamproites to 6.4 GPa and their bearing on the sources of lamproites magmas. Mineralogy and Petrology 74, 115–128.

O'Neil, H.C., 1981. The transition between spinel lherzolite and garnet lherzolite, and it use as geobarometer. Contributions to Mineralogy and Petrology 77, 185–194.

Palomeras, I., Thurner, S., Levander, A., Liu, K., Villasenor, A., Carbonell, R., Harnafi, M., 2014. Finite-frequency Rayleigh wave tomography of the western Mediterranean: mapping its lithospheric structure. Geochemistry, Geophysics, Geosystems 15, 140–160.

Pérez-Peña, J.V., Azor, A., Azañón, J.M., Keller, E.A., 2010. Active tectonics in the Sierra Nevada (Betic Cordillera, SE Spain): insights from geomorphic indexes and drainage pattern analysis. Geomorphology 119 (1–2), 74–87.

Pérez-Valera, L.A., Rosenbaum, G., Sánchez-Gómez, M., Azor, A., Fernández-Soler, J.M., Pérez-Valera, F., Vasconcelos, P.M., 2013. Age distribution of lamproites along the Socovos Fault (southern Spain) and lithospheric scale tearing. Lithos 180-181, 252–263.

Philpotts, A.R., 1990. Principles of Igneous and Metamorphic Petrology. Cambridge University Press, Cambridge (498 pp.).

Platt, J.P., Behr, W.M., Johanesen, K., Williams, J.R., 2013. The betic-Rif arc and its orogenic hinterland: a review. Annual Review of Earth and Planetary Sciences 41, 313–357.

Playà, E., Gimeno, D., 2006. Evaporite deposition and coeval volcanism in the Fortuna Basin (Neogene, Murcia, Spain). Sedimentary Geology 188-189, 205–218.

Prelević, D., Foley, S.F., 2007. Accretion of arc-oceanic lithospheric mantle in the Mediterranean: evidence from extremely high-Mg olivines and Cr-rich spinel inclusions from lamproites. Earth and Planetary Science Letters 256, 120–135.

Prelević, D., Foley, S.F., Romer, R., Conticelli, S., 2008. Mediterranean tertiary lamproites derived from multiple source components in postcollisional geodynamics. Geochimica et Cosmochimica Acta 72, 2125–2156.
Prelević, D., Akal, C., Romer, R., Foley, S.F., 2010a. Lamproites as indicators of accretion and/or shallow subduction in the assembly of south-western Anatolia, Turkey. Terra Nova 22, 443–452.
Prelević, D., Stracke, A., Foley, S.F., Romer, R.L., Conticelli, S., 2010b. Hf isotope compositions of Mediterranean lamproites: mixing of melts from asthenosphere and crustally contaminated mantle lithosphere. Lithos 119, 297–312.
Prelević, D., Jacob, D.E., Foley, S.F., 2013. Recycling plus: a new recipe for the formation of Alpine-Himalayan orogenic mantle lithosphere. Earth and Planetary Science Letters 362, 187–197.
Righter, K., Carmichael, I.S.E., 1996. Phase equilibria of phlogopite lamprophyres from western Mexico: biotite-liquid equilibria and P–T estimates for biotite-bearing igneous rocks. Contributions to Mineralogy and Petrology 123, 1–21.
Rock, N.M.S., 1991. Lamprophyres. Blackie, Glasgow (285 pp.).
Rosenbaum, G., Lister, G.S., 2004. Neogene and quaternary rollback evolution of the Tyrrhenian Sea, the Apennines, and the Sicilian Maghrebides. Tectonics 23, TC1013.
Royden, L., 1993. Evolution of retreating subduction boundaries formed during continental collision. Tectonics 12, 629–638.
Sanz de Galdeano, C., Vera, J.A., 1992. Stratigraphic record and palaeogeographical context of the Neogene basins in the Betic Cordillera, Spain. Basin Research 4, 21–36.
Schmidt, K.H., Bottazzi, P., Vannucci, R., Mengel, K., 1999. Trace element partitioning between phlogopite, clinopyroxene and leucite lamproite melt. Earth and Planetary Science Letters 168, 287–299.
Seghedi, I., Szakács, A., Pacheco, A.H., Matesanz, J.L.B., 2007. Miocene lamproite volcanoes in south-eastern Spain — an association of phreatomagmatic and magmatic products. Journal of Volcanology and Geothermal Research 159 (1–3), 210–224.
Semiz, B., Çoban, H., Roden, M.F., Özpinar, Y., Flower, M.F.J., McGregor, H., 2012. Mineral composition in cognate inclusions in Late Miocene–Early Pliocene potassic lamprophyres with affinities to lamproites from the Denizli region, Western Anatolia, Turkey: implications for uppermost mantle processes in a back-arc setting. Lithos 134-135, 253–272.
Soto, J.I., Fernández-Ibáñez, F., Fernández, M., García-Casco, A., 2008. Thermal structure of the crust in the Gibraltar arc: influence on active tectonics in the western Mediterranean. Geochemistry, Geophysics, Geosystems 9, Q10011.
Spera, F.J., 1987. Dynamics and translithospheric migration of metasomatic fluid and alkaline magma. In: Menzies, M.A., Hawkesworth, C.J. (Eds.), Mantle Metasomatism. Academic Press Geology Series, London, pp. 1–18.
Streck, M., 2008. Mineral textures and zoning as evidence for open system processes. Reviews in Mineralogy and Geochemistry 69, 595–622.
Takahashi, E., 1986. Melting of a dry peridotite KLB-1 up to 1.4 GPa: implications on the origin of peridotite upper mantle. Journal of Reophysical Research 91, 9367–9382.
Thurner, S., Palomeras, I., Levander, A., Carbonell, R., Lee, C.-T., 2014. Ongoing lithospheric removal in the western Mediterranean: evidence from Ps receiver functions and thermobarometry of Neogene basalts (PICASSO project). Geochemistry, Geophysics, Geosystems 15, 1113–1127.
Toscani, L., Contini, S., Ferrarini, M., 1995. Lamproitic rocks from Cabezo Negro de Zeneta: Brown micas as a record of magma mixing. Mineralogy and Petrology 55 (4), 281–292.
Turner, S.P., Platt, J.P., George, R.M.M., Kelley, S.P., Pearson, D.G., Nowell, G.M., 1999. Magmatism associated with orogenic collapse of the betic–Alboran domain, SE Spain. Journal of Petrology 40, 1011–1036.
Ubide, T., Galé, C., Arranz, E., Lago, M., Larrea, P., 2014a. Clinopyroxene and amphibole crystal populations in a lamprophyre sill from the Catalonian Coastal Ranges (NE Spain): a record of magma history and a window to mineral-melt partitioning. Lithos 184-187, 225–242.
Ubide, T., Galé, C., Larrea, P., Arranz, E., Lago, M., 2014b. Antecrysts and their effect on rock compositions: the Cretaceous lamprophyre suite in the Catalonian Coastal Ranges (NE Spain). Lithos 206-207, 214–233.
Vaughan, A.P.M., Scarrow, J.H., 2003. K-rich mantle metasomatism control of localization and initiation of lithospheric strike-slip faulting. Terranova 15 (3), 163–169.
Venturelli, G., Capedri, S., Di Battistini, G., Crawford, A., Kogarko, L.N., Celestini, S., 1984. The ultrapotassic rocks from southeastern Spain. Lithos 17, 37–54.
Venturelli, G., Salvioli-Mariani, E.S., Foley, S.F., Capedri, S., Crawford, A.J., 1988. Petrogenesis and conditions of crystallization of Spanish lamproitic rocks. The Canadian Mineralogist 26, 67–79.
Venturelli, G., Toscani, L., Salvioli-Mariani, E., 1991. Mixing between lamproitic and dacitic components in Miocene rocks of SE Spain. Mineralogical Magazine 55, 282–285.
Wan, Z.A., Coogan, L.A., Canil, D., 2008. Experimental calibration of aluminum partitioning between olivine and spinel as a geothermometer. American Mineralogist 93, 1142–1147.
Xu, Y., Huang, X., Menzies, M.A., Wamg, R., 2003. Highly magnesian olivines and green-core clinopyroxenes in ultrapotassic lavas from western Yunnan, China: evidence for a complex hybrid origin. European Journal of Mineralogy 15, 965–975.
Zeck, H.P., Williams, I.S., 2002. Inherited and magmatic zircon from Neogene Hoyazo cordierite dacite, SE Spain—anatectic source rock provenance and magmatic evolution. Journal of Petrology 43, 1089–1104.
Zeck, H.P., Kristensen, A.B., Williams, I.S., 1998. Post-collisional volcanism in a sinking slab setting-crustal anatectic origin of pyroxene-andesite magma, Caldear Volcanic Group, Neogene Alborán volcanic province, southeastern Spain. Lithos 45 (1–4), 499–522.